博士論文

Investigation on improving performance of parametric array

(パラメトリックアレイの高性能化に関する研究)

東京大学大学院新領域創成科学研究科

海洋技術環境学専攻

藤澤 慶

ABSTRACT

This paper presents an investigation on the parametric sound enhancement at the sum and difference frequencies through different fluid layers to improve the performance of parametric array. To predict the parametric sound enhancement through different fluids, theoretical and numerical model are newly developed. Theoretical analysis is based on the Burgers equation with transmittance boundary condition and it is solved by quasi-linear approximation method. Numerical simulation is conducted by the hybrid model which combines the fluid dynamic equations in the vicinity of sound source and the KZK equation in the far field. This accounts for the effects of diffraction, absorption and nonlinearity during sound propagation in the fluids with transmission loss at the different fluid layer boundaries. The theoretical analysis and the numerical model are used to investigate the secondary wave generations including parametric sound at the sum and difference frequencies with and without different fluids in water environment. The generations of the secondary waves with respect to the water (enhancement ratio) are studied. To confirm the theoretical and numerical results, experiments are carried out by hydrophone measurements. The results indicate that a different fluid layer with a length of 150 mm generates an amplitude 3.7 times larger at the difference frequency and 2.9 times larger at the sum frequency compared to that in water alone. This is due to the nonlinear fluid properties and diffraction effect in the different fluid layer. It was also found that the enhancement ratio at the sum and difference frequencies increased with increasing length of the different fluid layer, while the enhancement ratio is slightly affected by the initial water layer length variation. The concept of different fluid layers combined with a shadow method is applied to the noninvasive measurement of a target square cylinder in water. It was found that the parametric sound is magnified using an different fluid layer and the size measurement accuracy of the target structure in water was better than that of conventional nonlinear imaging.

Acknowledgment

List of content

List of Figures

List of Tables

Nomenclature

a: radius of sound source

c: sound speed

k: wave number

f: frequency

f_C: center frequency of primary frequencies

f_D: difference frequency

f_S: sum frequency

f_1, f_2: two primary frequencies

g, h: Fourier series coefficients

L_D: length of different fluid layer

p: sound pressure

p_0: input sound pressure

p_{max}: maximum sound pressure

R_d: Rayleigh distance

T: transmittance

t: time

r: radial distance

Z: acoustic impedance

z: axial distance

z_0: position of different fluid layer

Subscripts

$_{AL}$: properties of aluminum

$_{C}$: center

$_{D}$: different fluid layer

$_{E}$: ethanol

$_{in}$: input boundary

$_{out}$: output boundary

$_{R}$: rubber film

$_{W}$: water

Greek letters

α: absorption coefficient

β: nonlinear coefficient

η: enhancement ratio

ρ: density

ξ: dimensionless radial coordinate

σ: dimensionless axial coordinate

τ: normalized retarded time

Ω: computational domain

ω: angular frequency

1. Introduction

1.1 Parametric array

Nonlinear acoustic techniques utilizing secondary wave generation, such as harmonics and parametric sound at the sum and difference frequencies of transmitted sound, have been a powerful tool for acoustic imaging [1 - 4] and nondestructive testing [5 - 8] of target structures. This nonlinear technique improves acoustic imaging quality because it gives rise to high beam directivity and low imaging artifacts compared with linear acoustic techniques.

A parametric array is one of the nonlinear transduction mechanisms. It is characterized by low side lobe secondary waves at harmonics and the parametric sound at the sum and difference frequencies of the transmitted waves in comparison with linear sound at the same frequency. These secondary waves including parametric sound are generated through the nonlinear interaction of primary waves at two different frequencies in the medium fluid, as reported by Westervelt [9] and Berktay [10]. These results indicate that the difference frequency wave generated from the parametric array contributes to a narrow, nearly side lobe free low frequency beam with a small sound absorption during long distance propagation. Later, Muir [11] showed that the narrower main lobe and lower side lobe of the parametric sound at the sum frequency compared to the transmitted primary waves in a water environment. This author also demonstrated the feasibility of using harmonics in imaging because of a narrower main lobe and a lower side lobe of the harmonics compared with the primary wave [12]. It should be noted that the sum frequency wave is useful when combined with a frequency compounding technique to reduce speckle noise in imaging, owing to a large number of secondary waves in the limited

bandwidth of a hydrophone [3, 13]. In addition, the secondary waves reduce reverberation artifacts in imaging. Since then, secondary waves at harmonics and the sum and difference frequency have been applied to the detection of embedded archaeological objects and sediment characterization [14, 15], medical imaging [2, 13, 16, 17, 18], underwater acoustic measurement [1, 3, 19, 20, 21] and seafloor characterization [22, 23]. Nonlinear acoustic imaging using secondary waves is known to improve the measurement accuracy and reduce reverberation artifacts compared with conventional linear acoustic techniques using primary waves.

Several numerical and experimental results for the enhancement of secondary waves, including harmonics and parametric sound, have been reported based on beam focusing with focused apertures [24] and phased arrays [25, 26]. However, by those experimental techniques it is difficult to obtain long distance enhancement with high directivity of the secondary waves due to the large diffraction in the far field. On the other hand, it is known that long distance enhancement of the difference frequency is obtained via a micro-bubble layer [27] which exhibits a large nonlinear oscillation on sound propagation [28, 29]. However, this micro-bubble layer largely broadens the beam directivity at the difference frequency compared to water [30]. An experimental technique for enhancing parametric sound using a silicon rubber material was also reported [31]. This technique, however, is difficult to apply to a high frequency wave because of the high sound absorption of silicon rubber in high frequencies.

1.2 Parametric sound enhancement

One of the important material properties of nonlinear sound generation including parametric sound generation is the ratio B/A (= $2(\beta - 1)$, β: nonlinear coefficient), that has its origin in the Taylor series expansion of the pressure variation in terms of density variations. This property has large influence on the generation of the secondary waves including parametric sound at the sum and difference frequency, which will be described in detail in Section 4.2. Several studies measured the harmonic generation to evaluate B/A in fluids which is called finite amplitude method [32], and those techniques showed that the ratio B/A of water is between 4 and 6, which is smaller than other liquid such as ethanol and acetone [33 - 35]. Therefore the nonlinear acoustic effects in water are small compared to other fluid materials, while such previous studies focused on measuring the ratio B/A for material characterization. To apply this phenomenon to noninvasive measurement and acoustic imaging as underwater technology, it is important to understand the enhancement area after the different fluid material with large nonlinear property and the acoustic beam characteristic of generated secondary waves. Moreover, it is important to understand the generation of parametric sound at the sum and difference frequency which is more widely used than that of harmonics in underwater acoustic imaging. Therefore, further studies on the enhancement of the parametric sound at the sum and difference frequency using different fluid layers and its application are of timely interest.

The purpose of this paper is to study the concept of different fluid layers in water to improve the enhancement of the parametric sound at the sum and difference frequency and apply to noninvasive measurement in water. Theoretical, numerical and experimental studies are carried out in this paper to verify the experimental techniques of using different fluid layer in water with

the parametric array and to understand the mechanism of parametric sound enhancement through different fluid layers. Furthermore, together with a shadow imaging technique, this enhancement technique is applied to the noninvasive detection of underwater structures.

1.3 List of publications

This thesis is based on the following five papers.

1. Fujisawa, K., & Asada, A. (2016). Nonlinear parametric sound enhancement through different fluid layer and its application to noninvasive measurement. *Measurement*, *94*, 726-733.
2. Fujisawa, K., & Asada, A. (2016). Nonlinear Acoustic Shadow Method to Reduce Reverberation Artifact. *Journal of Flow Control, Measurement & Visualization*, *4*(02), 49.
3. Fujisawa, K., & Asada, A. (2015). Numerical method for calculating nonlinear sound propagation in full acoustic field. *Acoustical Science and Technology*, *36*(5), 438-440.
4. Fujisawa, K., & Asada, A. (2015). Nonlinear sound propagation on acoustic phased array. *Applied Acoustics*, *95*, 57-59.
5. Fujisawa, K. (2014). Numerical Study on Nonlinear Sound Propagation for Parametric Array. *Journal of Flow Control, Measurement & Visualization*, *2014*.

2. Theory

Figure 1 shows the illustration of the concept of parametric sound enhancement through different fluids in water environment and its application to noninvasive measurement of underwater structures [36]. To understand the parametric sound enhancement in different fluid layers, the simple theoretical model is introduced to estimate the enhancement ratio of the secondary wave including harmonics and the parametric sound at the sum and difference frequencies. It should be noted that this theoretical model focuses on characterizing the influence of the fluid layer properties in water on the enhancement of the parametric sound.
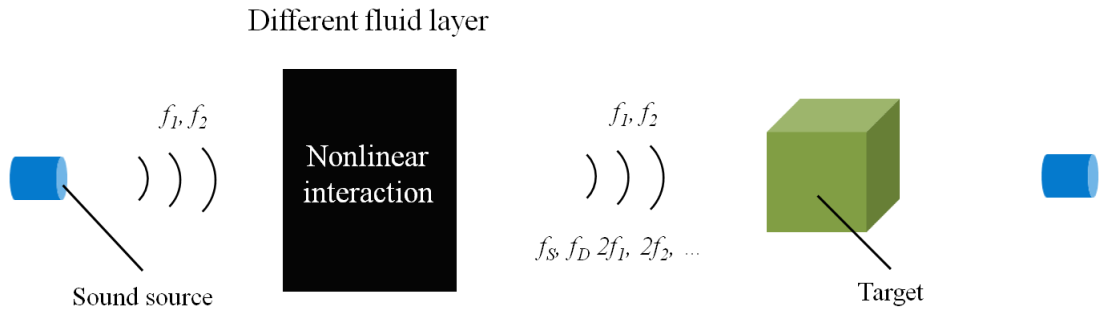
Figure 1 Nonlinear parametric sound enhancement through different fluids and its application to noninvasive detection of underwater structures.

2.1 Parametric sound generation

The theoretical consideration is based on the Burgers equation for a large Goldberg's number in sound propagations [37, 38]. The governing equation is given by Equation 1. Note that the nonlinear term which is related to the generation of secondary waves is underlined in the governing equation.

$$\frac{\partial p}{\partial z} - \frac{\beta}{2\rho c^3}\frac{\partial p^2}{\partial \tau} = 0 \qquad \text{Equation 1}$$

2.Theory

$$\tau = t - \frac{z}{c}$$

Equation 2

where c is the sound speed, p is the sound pressure, t is time, z is the propagation distance, β ($= 1 + 0.5$ B/A) is the nonlinear coefficient, ρ is the fluid density and τ is the retarded time. Although this equation approximates nonlinear sound propagation as plane wave without diffraction and absorption, it considers the major influence of fluid properties on nonlinear sound propagation. The initial condition for this equation is given by

$$p = p_0\left(sin\omega_1 t + sin\omega_2 t\right)$$

Equation 3

where p_0 is the input sound pressure of the primary waves at two angular frequencies (ω_1 and ω_2) to generate parametric sound at the sum ($= \omega_1 + \omega_2$) and difference angular frequencies ($= \omega_1 - \omega_2$). Quasi-linear approximation method (successive approximation for weak nonlinearity) was used to derive the sound pressure of the secondary wave p_W using Equation 1 with the initial condition Equation 3 as sound source. In quasi-linear approximation method, transmitted primary waves propagate linearly without being affected by the presence of the secondary waves.

The sound pressure of the secondary wave in water can be obtained from the nonlinear term in Equation 1 as follows,

$$p_W = \frac{A}{2}\omega p_0^{\ 2}\sin \omega\tau$$

Equation 4

$$A = \chi_W z$$

Equation 5

$$\chi_W = \frac{\beta_W}{\rho_W c_W^{\ 3}}$$

Equation 6

6

2.Theory

where ω is the angular frequency of the secondary wave and the subscript $_W$ denotes the properties of water. It should be noted that A in Equation 4 has a positive sign for the sum frequency wave, a negative sign for the difference frequency wave, and $A = \chi_W z/2$ for harmonics.

To derive the sound pressure of secondary waves p_D through the different fluid, we divide the computational domain into two different computational region of water and different fluid layer. At different fluid/water interfaces, reflection and transmission at the interface is caused by an acoustic impedance difference. In the theoretical consideration, the sound pressure transmittances of plane wave from water to different fluid T_{WD} and from different fluid to water T_{DW} can be written as,

$$T_{WD} = \frac{2\rho_D c_D}{\rho_W c_W + \rho_D c_D} \qquad \text{Equation 7}$$

$$T_{DW} = \frac{2\rho_W c_W}{\rho_D c_D + \rho_W c_W} \qquad \text{Equation 8}$$

where the subscript $_D$ denotes the fluid properties of the different fluid. This equation uses the assumption of the plane wave propgation. In case of water-ethanol-water condition with rubber film between water and ethanol, the transmittances of the sound pressure are given as:

$$T_{WD} = \frac{4\rho_R c_R \rho_E c_E}{\left(\rho_W c_W + \rho_R c_R\right)\left(\rho_R c_R + \rho_E c_E\right)} \qquad \text{Equation 9}$$

$$T_{DW} = \frac{4\rho_R c_R \rho_W c_W}{\left(\rho_E c_E + \rho_R c_R\right)\left(\rho_R c_R + \rho_W c_W\right)} \qquad \text{Equation 10}$$

where the subscripts $_E$ and $_R$ denote the material properties of the ethanol and

rubber, respectively. Then, the sound pressure p_D of a secondary wave through the different fluid layer in water is written as,

$$p_D = \frac{A_1 + A_2 + A_3}{2} \omega \, p_0{}^2 \sin \omega \tau \qquad \text{Equation 11}$$

$$A_1 = T_{DW} T_{WD} \chi_W z_0 \qquad \text{Equation 12}$$

$$A_2 = T_{DW} T_{WD}{}^2 \chi_D L_D \qquad \text{Equation 13}$$

$$A_3 = T_{WD}{}^2 T_{DW}{}^2 \chi_W \left(z - z_0 - L_D \right) \qquad \text{Equation 14}$$

$$\chi_D = \frac{\beta_D}{\rho_D c_D{}^3} \qquad \text{Equation 15}$$

where A_1 represents the nonlinear effect caused by propagation in water between the transducer and different fluid, A_2 represents the effect caused by propagation in the different fluid, A_3 represents the effect caused by propagation in water beyond the different fluid, and z_0 and L_D are the lengths of the water layer near the transducer and different fluid layer, respectively.

2.2 Enhancement ratio

In order to understand the nonlinear effect in the different fluid layer as a function of propagation distance from sound source, the ratio of the sound pressure through the different fluid layer and water is defined as,

$$\eta = \frac{p_D}{p_W} \qquad \text{Equation 16}$$

When $\eta > 1$, the sound pressure of the secondary wave through the different

2.Theory

fluid layer becomes larger than that in water, which suggests an enhancement of sound pressure caused by the different fluid layers. The enhancement ratio through the different fluid layer in water is obtained by substituting Equations 4-15 into Equation 16, yielding,

$$\eta = \frac{T_{DW}\left(T_{WD}\chi_W z_0 + T_{WD}{}^2 \chi_D L_D\right) + \left(T_{WD}T_{DW}\right)^2 \chi_W L_W}{\chi_W z}$$

Equation 17

$$L_W = z - z_0 - L_D$$

Equation 18

Equation 17 indicates that the enhancement ratio η is not affected by the frequencies and sound pressure of the primary and secondary waves in plane wave without abosrption during sound propagation. Therefore, the present result is applicable to the secondary waves of parametric sound at the sum and difference frequencies and harmonics. Note that the enhancement ratio η in the different fluid layer was calculated by setting $T_{DW} = 1$ and $L_W = 0$ in Equation 17. It should be noted that the sound attenuation caused by absorption in fluid which reduces the generation of the secondary waves are assumed to be small in the derivation of this model. Moreover, this model is not valid for sound propagation beyond the distance where shock waves are generated, because the model uses the quasi-linear approximation which is limitted to the weak nonlinear phenomena.

A theoretical consideration for achieving high enhancement of the parametric sound through the different fluid layer in water was carried out for five types of fluids, i.e., benzene, silicon oil, acetone, hexane, and ethanol. Fluid properties, such as sound speed c, nonlinear coefficient β and density ρ of the five fluids are listed in Table 1. It also provides the theoretical results of the enhancement ratio η for the reference case of $L_D = 150$ mm for each fluid layer and $z_0 = 20$ mm in water just behind the rubber film. The results show an

increase in the enhancement ratio η of each fluid compared with water. Although a high enhancement ratio was obtained for the cases of ethanol, hexane and acetone, the highest enhancement ratio was obtained for ethanol. It should be noted that the high enhancement ratio in ethanol is caused by the high nonlinear coefficient of the fluid. The enhancement ratio also depends on the length of the different fluid layer, which will be discussed in the following section.

Figure 2 shows variations of the enhancement ratio η of the different fluid layers in water, plotted against the axial distance z from the parametric array. For $z > z_0$, Equation 17 can be rewritten as,

$$\eta = \eta_1 + \eta_2 + \eta_3 \qquad\qquad \text{Equation 19}$$

$$\eta_1 = \left(T_{WD}T_{DW}\right)^2 \qquad\qquad \text{Equation 20}$$

$$\eta_2 = \frac{T_{DW}\left(T_{WD}\chi_W z_0 + T_{WD}{}^2 \chi_D L_D\right)}{\chi_W z} \qquad\qquad \text{Equation 21}$$

$$\eta_3 = \frac{-\left(T_{WD}T_{DW}\right)^2 \chi_W \left(z_0 + L_D\right)}{\chi_W z} \qquad\qquad \text{Equation 22}$$

This explains the decrease in $1/z$ for $z > z_0 + L_D$, and the asymptotic value of η is $(T_{WD}T_{DW})^2$. As z increases, the nonlinear contribution of the fluid becomes negligible and only the interfaces affect η. The enhancement ratio η is smaller than unity at the water/fluid interface ($z = z_0$) because of the smaller impedance of the different fluid ($T_{WD} < 1$). Then, η increases rapidly and then gradually as the distance z increases to the end of the fluid layer. At the fluid/water interface ($z = 170$ mm), η rapidly increases because of the larger acoustic impedance to water compared with the different fluid medium ($T_{DW} > 1$). Finally, η gradually decreases in water as the distance z increases. Note that the discontinuities of the enhancement ratio η at the interfaces reflect the distinct properties of the fluids.

2.Theory

The theoretical consideration of the interface effect indicates that, among the five fluids used, the highest enhancement ratio is obtained for the ethanol layer as summarized in Table 1.

Figure 3 shows the variations of the enhancement ratio η with respect to the propagation distance z for various lengths of the ethanol layer in water, with the length of the initial water layer set to a fixed $z_0 = 20$ mm in all cases. The maximum enhancement ratio η_{max} was measured in water at the fluid interface $L_W = 0$, and η_{max} can be expressed as

$$\eta_{\max} = T_{DW}\left(\frac{T_{WD}z_0}{z_0 + L_D} + \frac{T_{WD}^2 \chi_D L_D}{\chi_W(z_0 + L_D)}\right) \qquad \text{Equation 23}$$

which implies that when L_D increases, η tends towards the asymptotic enhancement ratio η_{asy} as

$$\eta_{asy} = \frac{T_{DW}T_{WD}^2 \chi_D}{\chi_W} \qquad \text{Equation 24}$$

Hence, the enhancement ratio η increases as the length of the ethanol layer L_D increases because of the larger influence of the ethanol layer, while the enhancement ratio seems to be saturated in an ethanol layer longer than $L_D = 200$ mm. The result indicates that the enhancement ratio of the ethanol layer is approximately 3, demonstrating that the experimental technique of using a different fluid layer in water can significantly enhance the signal amplitudes of the secondary waves from the parametric array. The nonlinear coefficient β, sound speed c and density ρ for the different fluid layer contribute to the enhancement ratio η of the secondary waves. Their contributions can be ranked as $c > \beta > \rho$ in the range of the present study. However, the contribution of the different fluid layer length L_D is dominant in the range of $L_D < 150$, while the

11

length effect is limited to a small fluid layer length because of the saturation behavior in longer length. Moreover, the different fluid layer should be placed close to the transducer for a sufficient length of the different fluid layer.
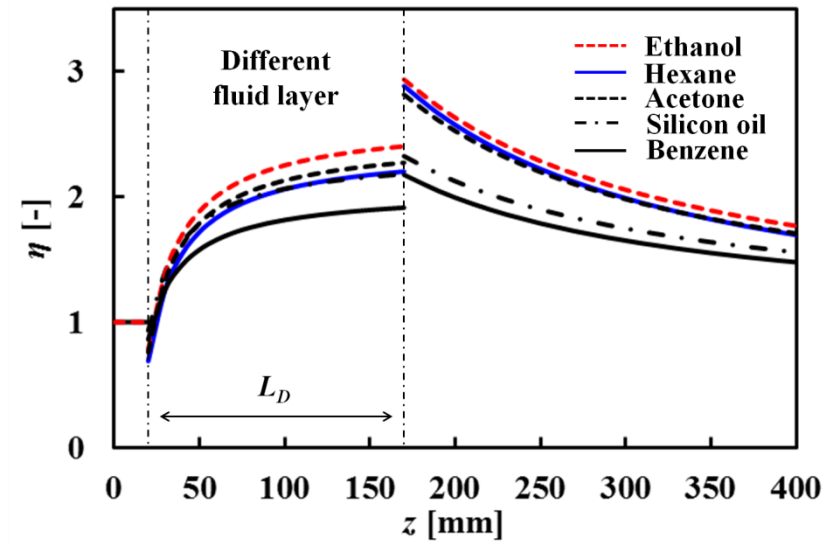
Figure 2 Variation of η for various fluid properties.
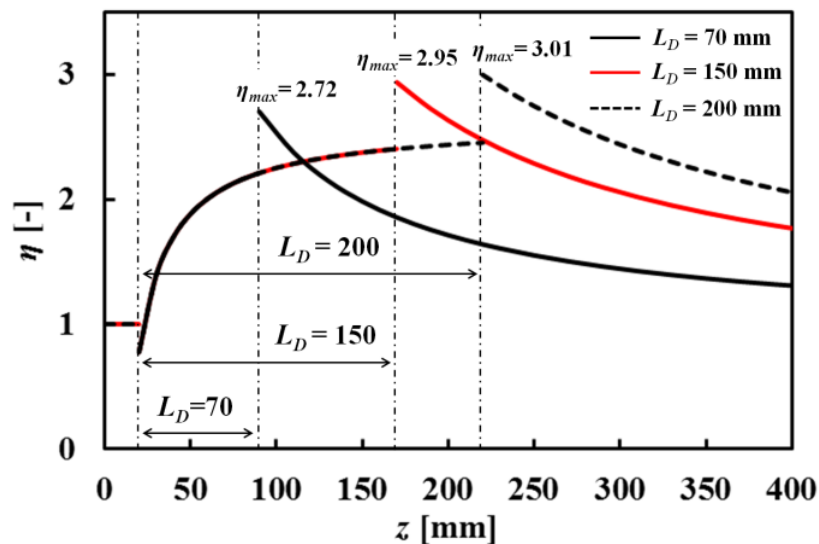
Figure 3 Variation of η for various L_D.

Table 1 Physical properties for theoretical calculation. Note that η_{max} (150) and η_{asy} denote the maximum enhancement ratio for L_D = 150 mm and the asymptotic enhancement ratio, respectively.

Name	β [-]	ρ [kg/m³]	c [m/s]	η_{max} (150) [-]	η_{asy} [-]
Water	3.5	998	1498	1	1
Benzene	5.5	874	1298	2.18	2.34
Silicone oil	6.7	970	1350	2.32	2.50
Acetone	5.6	785	1170	2.81	3.06
Hexane	6.0	655	1203	2.88	3.15
Ethanol	6.3	789	1207	2.95	3.22

3. Experiments

To confirm the theoretical results, the parametric sound enhancement through different fluid layers was measured by hydrophone and enhancement ratio was experimentally evaluated using sound pressure of the secondary waves including harmonics, and parametric sound at the sum and difference frequencies with and without different fluid layer. In this study, ethanol (C_2H_5OH) is used as different fluid, which showed the largest enhancement for the secondary waves among the five types of fluids as shown in Section 2.

3.1 Experimental condition

The sound pressure distributions through different fluid layer (ethanol) were measured using a calibrated hydrophone, as shown in Figures 4 (a) and (b). The water tank used in the experiments was 600 mm long, 500 mm wide, and 500 mm deep. It was filled with degassed and distilled water maintained at a temperature of 298 K. The different fluid layer was placed at a distance of z_0 away from the transducer in the water tank and the sound waves were measured by traversing the hydrophone using a three-dimensional positioning stage that had an accuracy of 0.05 mm. A cylinder with a radius R_C with a thin rubber film of thickness 0.1 mm contained ethanol to prevent any mixing of ethanol and water. Note that the sound absorbing materials were pasted on the inner surface of the cylinder and the water tank in order to minimize the reverberation waves. In the experiments, a circular type transducer with a flat surface was used as a sound source. In this study, the received signals were averaged over 64 times at each position to increase the experimentally attained signal-to-noise ratio.

3. Experiments
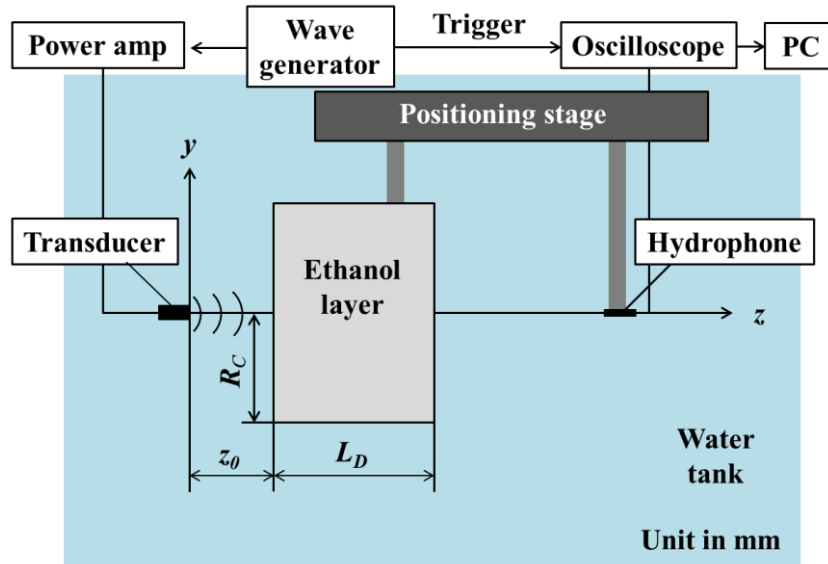
(a)
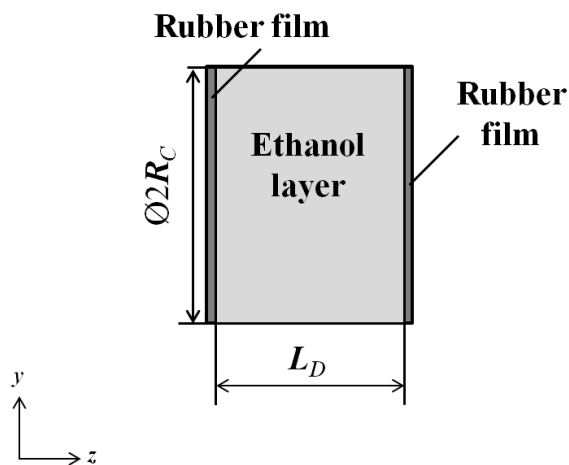
(b)

Figure 4 Experimental setup for parametric sound propagation through different fluids.

3.2 Experimental results

Experiments were carried out for the ethanol layer which was set in a water environment at a distance $z_0 = 20$ mm away from the transducer. The lengths of the ethanol layer were set to either $L_D = 70$ mm or 150 mm. The size of cylinder was 120 mm in diameter. Furthermore, the rubber film effect on η of higher harmonics and sum frequency can be minimized by dividing the sound pressure through the different fluid for a secondary wave by that through the water layer with the rubber film. The transducer used in the experiment was a circular type transducer which was 12 mm in diameter with a flat surface (Japan Probe B2K10I) and center frequency of 2.0 MHz. Ethanol was confined to the circular cylindrical housing that had an inner diameter of 120 mm. The receiver hydrophone (Japan Probe B5K5I) had a flat frequency response over the frequency range from 2 to 8 MHz. The transducer was excited by two different frequencies of $f_1 = 2$ MHz and $f_2 = 2.4$ MHz as the primary waves with a transmittance time of 15 μs. In this experiment, the sum frequency wave and harmonics were considered because of the limitations on receiving hydrophone performance for the difference frequency wave. However, the results are expected to be valid for the difference frequency wave within the range considered in the theoretical model.

Figures 5 (a) and (b) show the waveforms of the sound signals from the hydrophone located at $z = 200$ mm with and without the ethanol layer in water, respectively. Note that the experiment is carried out at the distance $z_0 = 20$ mm and the ethanol layer is set to $L_D = 150$ mm. The same input voltage was applied to the transducer in both cases. The results show that when compared with the waveform observed for water, waveform distortions were observed for the ethanol layer because of the secondary wave generations.
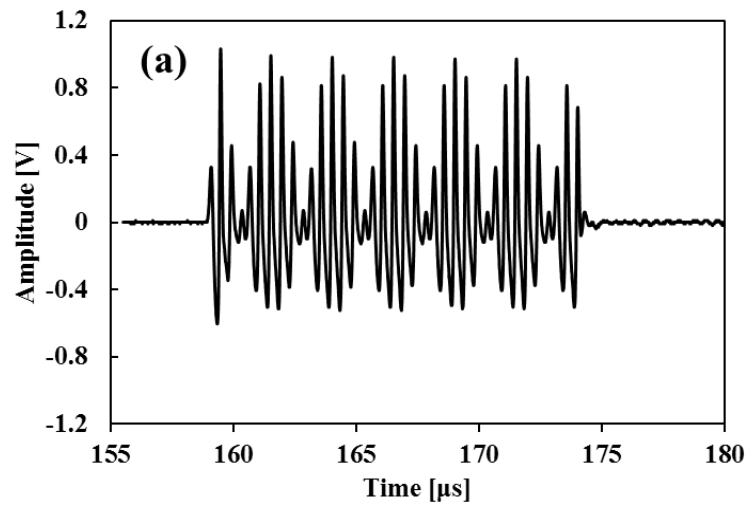
(a) Through ethanol layer
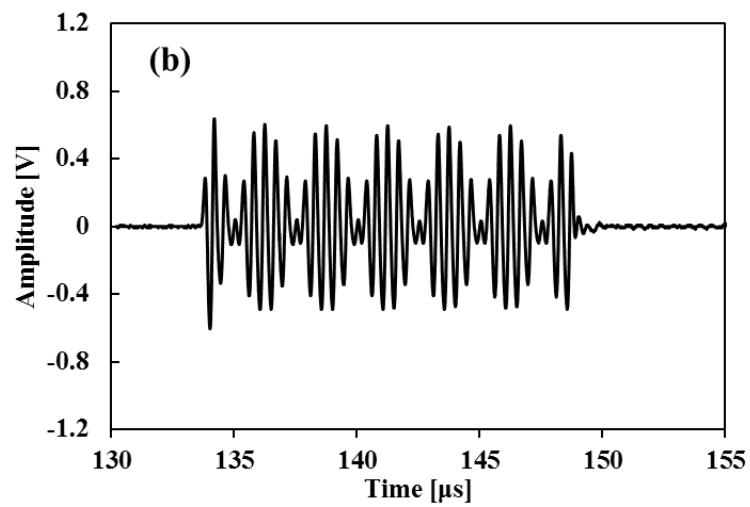
(b) Through water layer.

Figure 5 Signal waveforms of parametric sound detected at $z = 200$ mm.

3. Experiments

Figures 6 (a) and (b) show the frequency spectra of the sound signals from the hydrophone located at $z = 200$ mm with and without the ethanol layer in water, respectively. The results show the generations of the secondary wave at the sum frequency ($f = 4.4$ MHz) and harmonics ($f = 4$ MHz and 4.8 MHz) caused by nonlinear sound propagation. It should be noted that the sound pressure at the sum frequency in the ethanol layer is more than three times larger than that in the water layer. The amplitude of the sum frequency secondary wave is larger than that of the second harmonic waves, although the frequency is close. This is because the conversion efficiency from the primary waves is larger for the sum frequency secondary wave than that for the second harmonics, which was described in Section 2. It is also found that the sound pressure at higher harmonics, such as $f = 6.4$ MHz and 6.8 MHz, are observed in the ethanol layer, while they are not clearly observed in the water layer. These results indicate that the sum frequency secondary wave is highly magnified in the ethanol layer in comparison with the water layer.

Figure 7 shows comparisons between the theoretical enhancement ratio and the experimental one along the beam axis in the water behind the ethanol layer of $L_D = 150$ mm and $L_D = 70$ mm. Both results show a similar tendency to experimental results that decrease in η with increasing axial distance z, suggesting the validity of the present theoretical analysis. Generally, these results agree qualitatively with each other, while the theoretical result is smaller than the experimental one, which might be due to the difference in diffraction effects between the sound propagation in ethanol and water, which are not considered in the present model. In order to verify the repeatability of these experiments, the experiments were performed thrice with the same experimental conditions. The scattering of the results was ± 4 % from the average.

18
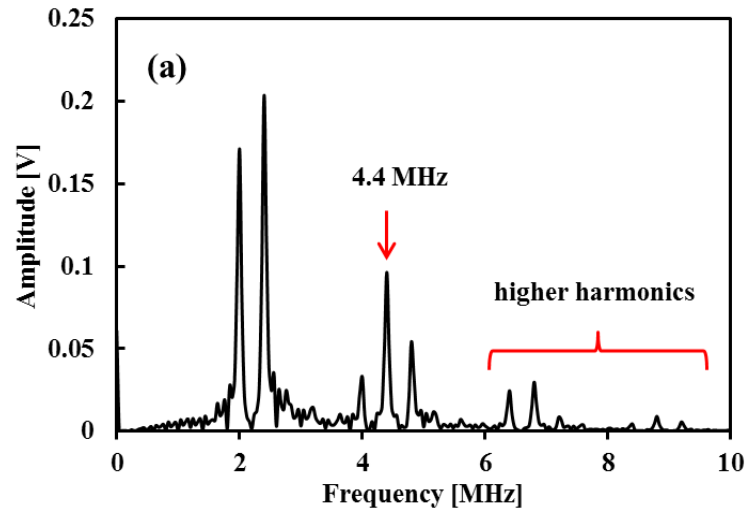
3. Experiments

(a) Through ethanol layer

(b) Through water layer.

Figure 6   Frequency spectra of parametric sound detected at $z = 200$ mm.
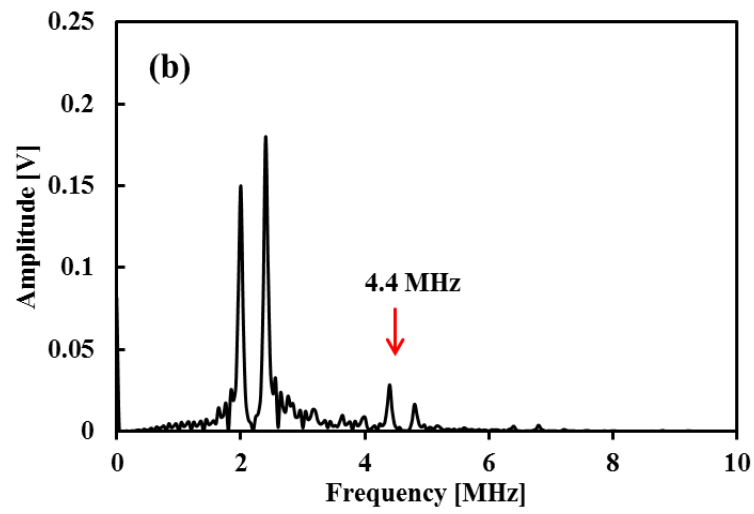
3. Experiments
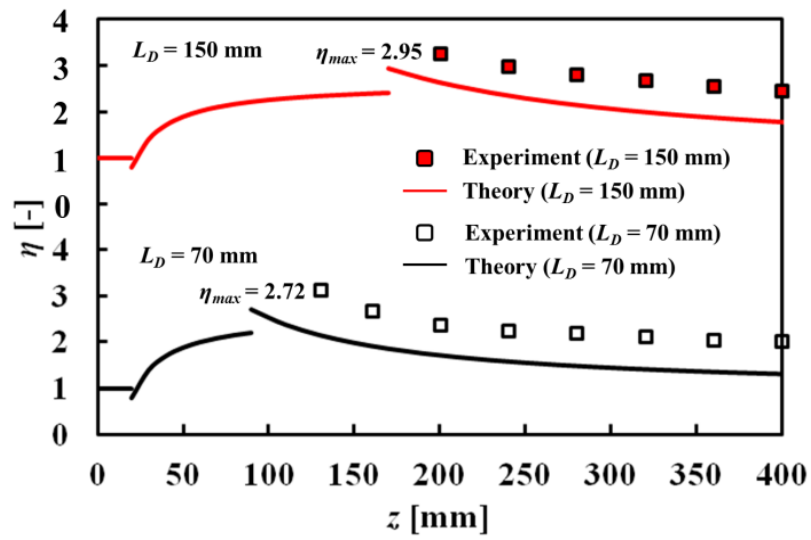
Figure 7 Variations of η with the axial distance z for L_D = 150 mm and 70 mm.

4. Numerical method

The theoretical analysis based on the Burgers equation is an efficient approach to predict the enhancement ratio of parametric sound through different fluid layer. However, it is difficult to understand the acoustic beam characteristic of the secondary waves in radial direction because of the plane wave approximation in the theoretical analysis. In this section, numerical method for nonlinear sound propagation through different fluid layers, called hybrid model, has been newly developed to study the parametric sound generation at the sum and difference frequencies in the different fluid layers.

4.1 Numerical method for nonlinear sound propagation

Nonlinear sound propagation in the far-field acoustics has been studied by numerically solving the Khokhlov-Zaboloskya-Kuznetsov (KZK) equation [39 - 41], which is derived from the fluid dynamic equations under the assumption of parabolic approximation. It is well known that the approach based on the KZK equation is efficient enough in the far-field acoustics, whereas it is not accurate enough in the near sound source owing to the parabolic nature of the equation [2, 42]. Therefore, the approach based on the KZK equation cannot be applied to nonlinear acoustics in the near field, where the reflection, refraction and interference of sound play an important role in the nonlinear sound propagation. Such a situation can be seen in applications, such as beam focusing by an acoustic phased array, and nonlinear sound propagation through different fluid layers. On the other hand, full-field (near- and far-field) acoustics can be studied by solving the fluid dynamic equations [26, 43 - 46]. This approach uses the compressible form of the fluid dynamic equations including the Navier-Stokes equation and those are solved numerically by the finite difference time domain (FDTD) method, although it requires a large amount of computational time even for a small target

area of computation. Therefore, it is difficult to simulate the full-field acoustics using this approach, especially in the huge target acoustic field of underwater acoustics. Note that solving the Westervelt equation is one of the numerical approaches, however large computational memory is required to solve the third order differential term in the equation [47].

4.2 Hybrid model

A novel numerical method for nonlinear sound propagation through different fluid layers, called 'hybrid model' is described, especially to consider the effect of reflection and refraction at the interface between two fluids, and the diffraction effect which generates the difference between the parametric sound at the sum and difference frequencies. It should be mentioned that the theoretical model based on the Burgers equation described in Section 2 neglects the diffraction effect during sound propagation. In the hybrid model, the velocity vector, and scalar values are expressed in axisymmetric cylindrical coordinates as shown in Figure 8, 9 and 10. This numerical model combines the fluid dynamic equations in the vicinity of sound source where the reflection, refraction and interference of sound play an important role in the propagation, and those are connected to the KZK equation in the far-field [48]. It should be noted that this numerical model focuses on predicting nonlinear sound distribution of parametric sound through different fluid layers in water.
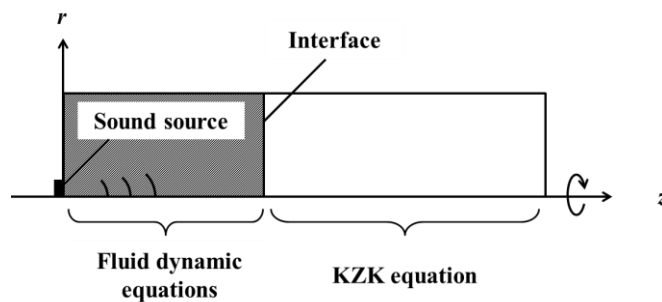
Figure 8 Axisymmetric simulation configuration. (hybrid model)

4.2.1 Fluid dynamic equations

Solving the fluid dynamic equations is one of the numerical approaches applicable to nonlinear sound propagation in full acoustic field in water. This approach considers the nonlinearity, dissipation, thermal conduction during the propagation in thermal viscous fluid by solving the continuity equation, the compressible form of the Navier-Stokes equation, the entropy balance equation, and the state equation,

$$\frac{D\rho}{Dt} + \rho \nabla \cdot \mathbf{u} = 0 \qquad \text{Equation 25}$$

$$\rho \frac{D\mathbf{u}}{Dt} + \nabla \cdot (P\mathbf{I} - \boldsymbol{\tau}) = 0 \qquad \text{Equation 26}$$

$$\rho T \frac{DS}{Dt} = \kappa \nabla^2 T + \boldsymbol{\tau} : \nabla \mathbf{u} \qquad \text{Equation 27}$$

$$\boldsymbol{\tau} = \left(\eta_B - \frac{2\mu}{3} \right)(\nabla \cdot \mathbf{u})\mathbf{I} + \mu \left(\nabla \mathbf{u} + (\nabla \mathbf{u})^{\mathrm{T}} \right) \qquad \text{Equation 28}$$

$$P^* = c^2 \rho^* + \frac{c^2 B}{2\rho_0 A} \rho^{*2} + \left(\frac{\partial P}{\partial s} \right)_{\rho,0} S^* \qquad \text{Equation 29}$$

where c: sound speed, t: time, P: pressure, S: entropy, T: temperature, κ: thermal conductivity, μ: shear viscosity, η_B: bulk viscosity, ρ: density, and $\mathbf{u}$: velocity vector. The index * expresses the fluctuation from the initial condition and the subscript 0 indicates the reference fluid properties at $T = 298$ K in atmospheric pressure.

$$P^* = P - P_0 = p \qquad \text{Equation 30}$$

4. Numerical method

$$\rho^* = \rho - \rho_0 \qquad \text{Equation 31}$$

$$S^* = S - S_0 \qquad \text{Equation 32}$$

These equations are solved by the finite difference time domain (FDTD) based method using staggered grids as shown in Fig 11. Staggered grid used in FDTD based method is different from a collocated grid, where all variables are stored in the same positions. In the FDTD based method, the leapfrog scheme is used for marching in time as shown in Fig 12. The increment of time step is determined to satisfy the Courant–Friedrichs–Lewy (CFL) condition. It should be mentioned that the 4_{th} order central difference scheme is applied to the acoustic terms, the QUICKEST scheme is used for the advection term, and the 4_{th} order central difference scheme is used for the dissipative terms. Note that this method was also applied to the prediction of nonlinear sound distribution of phased array as shown in Appendix A. This direct numerical approach, however, requires large computational cost, and the computational cost increases with increasing of computational area. Note that the effects of nonlinearity and absorption during sound propagation in rubber film is neglected in the numerical calculation because the length of the rubber film is smaller than wavelength. Therefore, B/A, η_B, μ and κ are set to 0 for the material properties for the calculation of sound propagation in rubber film in this calculation.
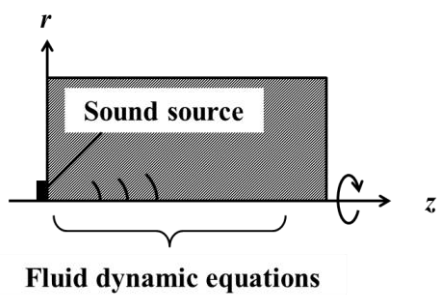
Figure 9 Axisymmetric simulation configuration. (Fluid dynamic equations)
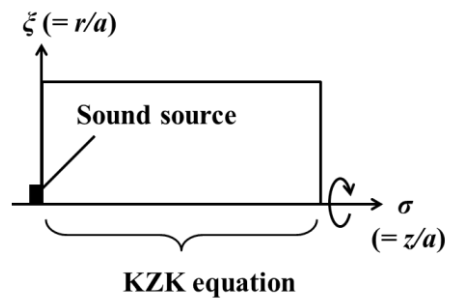
Figure 10 Axisymmetric simulation configuration. (KZK equation)
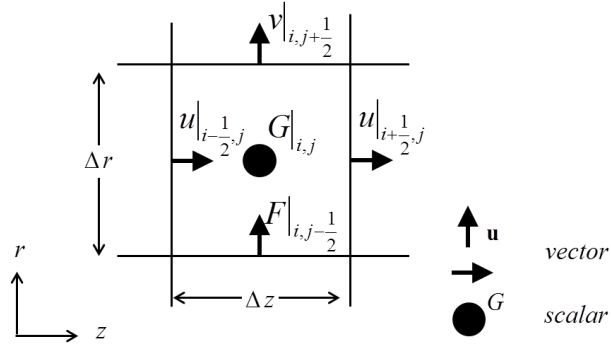
Figure 11 Staggered grid system.
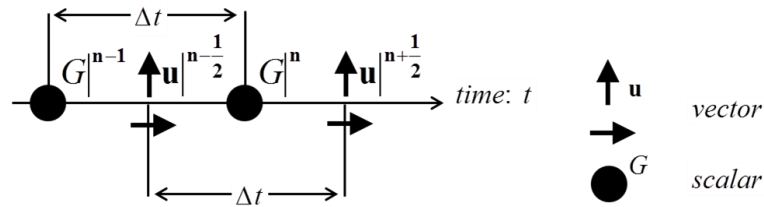
Figure 12 Leapfrog scheme.

4.2.2 Khokhlov - Zabolotskaya - Kuznetsov equation

For the calculation of the hybrid model for the nonlinear sound distribution in the far field, the KZK equation is numerically solved using the distribution of sound pressure obtained from the numerical simulation of the fluid dynamic equations. The KZK equation (Equation 33) is the parabolic equation that is commonly used in nonlinear sound propagation considering the nonlinearity, diffraction, and diffusivity of sound propagation. Note that the nonlinear term is underlined in Equation 33.

$$\frac{\partial^2 p*}{\partial \tau * \partial \sigma} - \alpha R_d \frac{\partial^2 p*}{\partial \tau *^2} - \frac{1}{2\sigma_D}\frac{\partial^2 p*^2}{\partial \tau *^2} - \frac{1}{4}\nabla_\perp^2 p* = 0 \qquad \text{Equation 33}$$

4. Numerical method

$$\nabla_{\perp}^{2} = \frac{\partial^{2}}{\partial \xi^{2}} + \frac{1}{\xi} \frac{\partial}{\partial \xi}$$

Equation 34

where a is the radius of sound source, k is the wave number, R_d $(= ka^2/2)$ is the Rayleigh distance, p_0 is the input sound pressure, $p*$ $(= p/p_0)$ is normalized sound pressure, z and r are the axial and radial distance, respectively, α is the absorption coefficient, β is the nonlinear coefficient, ρ is the density, σ $(= z/a)$ and ξ $(= r/a)$ are the dimensionless axial distance and radial distance, respectively, σ_D $(= \rho c^3/(R_d \beta p_0))$ is normalized shock wave formation distance, $\tau*$ $(= \omega (t - z/c))$ is normalized retarded time and ω is the angular frequency. The second and third term of Equation 33 represents the absorption and nonlinearity during sound propagation, respectively. The usage of the KZK equation for nonlinear sound propagation is accurate enough for most acoustic applications, while it is restricted to the region close to beam axis and relatively distant from a sound source. In addition, it is limited to the applications of one-way propagation due to the parabolic approximation.

The KZK equation is solved by the finite difference method in frequency domain after converting it into Fourier series equations. In the method, sound pressure $p*$ is described by following Fourier series,

$$p* = \sum_{n=1}^{\infty} \left(g_n \sin n\tau + h_n \cos n\tau \right)$$

Equation 35

where g_n and h_n are the Fourier series coefficients of n_{th} frequency components. To convert the KZK equation into Fourier series equations, substituting Equation 35 into Equation 33 yielding,

$$\frac{\partial g_n}{\partial \sigma} = A + \frac{n}{2\sigma_D} B$$

Equation 36

$$A = -\alpha_n R_d g_n + \frac{1}{4n} \nabla_{\perp}^{2} h_n$$

Equation 37

$$B = \frac{1}{2}\sum_{m=1}^{n-1}\left(g_m g_{n-m} - h_{n-m}h_m\right) - \sum_{m=n+1}^{\infty}\left(g_m g_{m-n} + h_m h_{m-n}\right)$$ Equation 38

$$\frac{\partial h_n}{\partial \sigma} = C + \frac{n}{2\sigma_D}\,D$$ Equation 39

$$C = -\alpha_n R_d h_n + \frac{1}{4n}\nabla_\perp^{\,2} g_n$$ Equation 40

$$D = \frac{1}{2}\sum_{m=1}^{n-1} g_m h_{n-m} - \sum_{m=n+1}^{\infty}\left(g_m h_{m-n} - g_{m-n}h_m\right)$$ Equation 41

where α_n is the absorption coefficient of n_{th} frequency components. Equations 36 and 39 are converted form of the KZK equation in frequency domain and those are solved by the implicit finite-difference method [41]. The term A in Equation 36 and the term C in Equation 39 represent the absorption and diffraction effect in sound propagation, respectively. The term B in Equation 36 and the term D in Equation 39 represent the nonlinearity of sound propagation, and those terms generate the secondary waves. In the method, sound pressure is periodic in time and the 46 different frequency components are solved in the present computation for parametric sound at the sum ($n = 23$) and difference frequency ($n = 1$).

4.2.3 Boundary conditions

The computational domain is surrounded by absorbing boundary to minimize acoustic reflections from the edges of the computational domain. For the computational domain solved by the fluid dynamic equations, the absorbing boundary is consisted of the fluid dynamic equations with artificial absorbing terms. The governing equations at the absorbing boundary are defined as follows,

$$\frac{D\rho}{Dt} + \rho\nabla\cdot\mathbf{u} + \underline{K\rho} = 0$$ Equation 42

4. Numerical method

$$\rho \frac{D\mathbf{u}}{Dt} + \nabla \cdot (P\mathbf{I} - \tau) + \underline{K\mathbf{u}} = 0 \qquad \text{Equation 43}$$

where K is the artificial absorption coefficient for the fluid dynamic equations [49]. Note that the artificial absorbing terms are underlined in Equation 42 and 43. The coefficient of artificial absorption can be defined as,

$$K = K_{max} \left(L_i / L_{AB} \right) \qquad \text{Equation 44}$$

where K_{max} is the maximum artificial absorption coefficient for the fluid dynamic equations, L_i and L_{AB} are the distance from the inlet of absorbing layer and the absorbing layer length, respectively. The sound pressure at the end of the computational domain in axial (Equation 45) and radial direction (Equation 46) are defined as follows,

$$p_i^{k+1} = p_{i-1}^k + \frac{c\Delta t - \Delta z}{c\Delta t + \Delta z} \left(p_{i-1}^{k+1} - p_i^k \right) \qquad \text{Equation 45}$$

$$p_j^{k+1} = p_{j-1}^k + \frac{c\Delta t - \Delta r}{c\Delta t + \Delta r} \left(p_{j-1}^{k+1} - p_j^k \right) \qquad \text{Equation 46}$$

where index i is the grid number in axial direction, index j is the grid number in radial direction and index k is the time increment.

In order to understand the effect of the absorbing boundary on sound propagation, the numerical simulation is carried out for the sound propagation emitted from circular disk of $a = 10$ mm in radius as shown in Figure 13. The sinusoidal plane wave is used as a sound source in water and the sound propagation in radial direction is neglected in the governing equations (= without diffraction effect). This corresponds to the one dimensional form of the fluid dynamic equations, where the frequency of sound source is set to $f = 1.1$ MHz and the pressure amplitude is set to 1 Pa in the present computation. The

28

4. Numerical method

computational domain is 80×80 mm in axial and radial directions, respectively, surrounded by absorbing boundary (Equation 42 and 43). Figure 14 shows the variation of sound pressure with K_{max} with the length of the absorbing layer: $L_{AB} =$ 50 mm. Sound absorption effect increases with increasing of K_{max}, while the numerical oscillations are generated in the case with $K_{max} = 1, 10, 1000$ and 10000 due to the small absorption effect or the large difference of K_{max} between absorbing boundary and water. Results with $K_{max} = 100$ shows the large absorption without reflection from the absorbing boundary.

Figure 15 shows the variation of sound pressure with the absorbing layer length: L_{AB} with $K_{max} = 100$. The results indicate that the sound pressure decreases in absorbing layer, while the results with $L_{AB} = 5, 10, 20$ show the numerical oscillations due to the reflection from the end of the absorbing boundary. On the other hand, the results with $L_{AB} = 50$ and 60 show no oscillation, while it increases the numerical cost. Therefore, the parameters of absorbing boundary are set to L_{AB} = 50 mm and $K_{max} = 100$ in the present calculation. For the comparative purpose, the numerical calcuation considering the sound propagation in radial direction (Fig 15 (b)) is carried out. It is found that the peak and dip of the sound pressure generated by the diffraction effect in the near field. Similarly to the result without diffraction effect, sound pressure attenuates as increasing of the propagation distance.
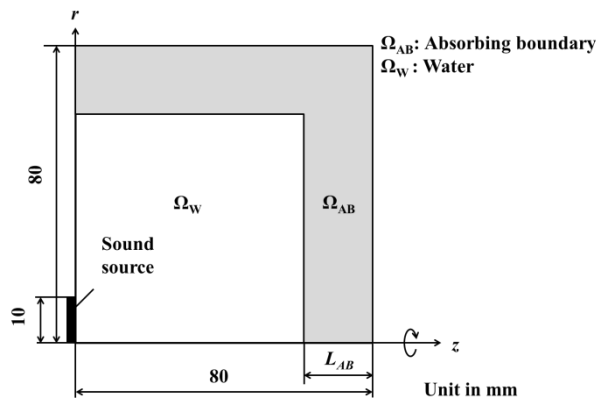
Figure 13 Schematic description of absorbing boundary.

4. Numerical method
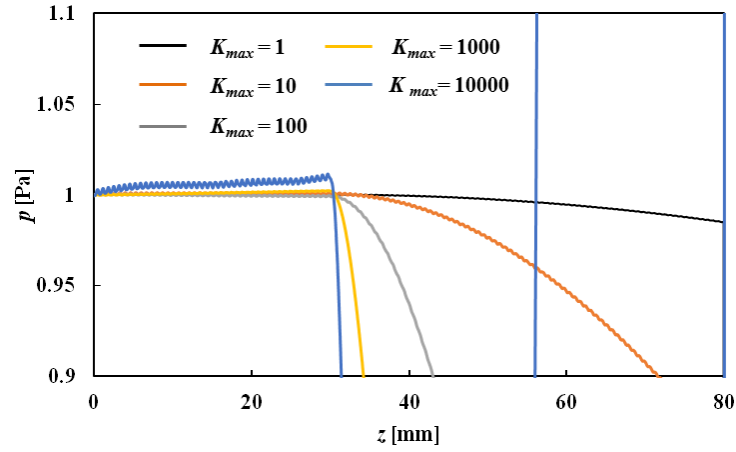
Figure 14 Variation of sound pressure with K_{max}.
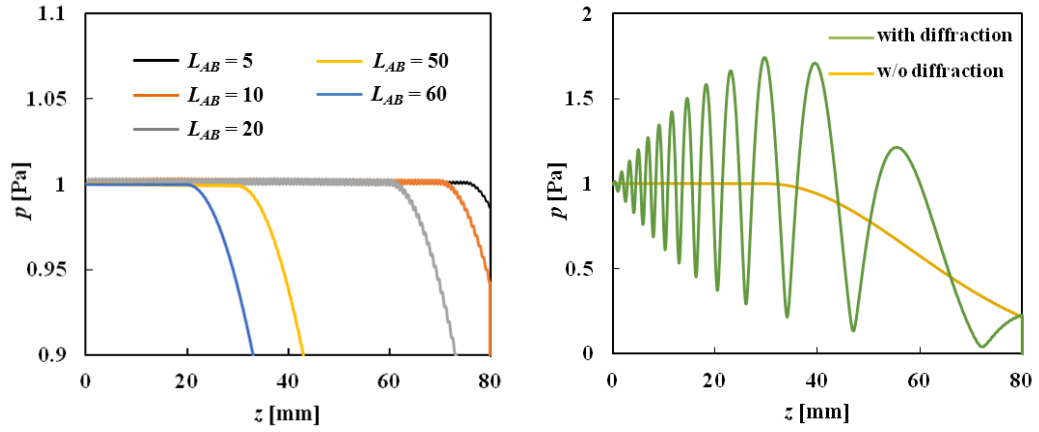
(a) without diffraction effect   (b) with diffraction effect

Figure 15 Variation of sound pressure with L_{AB}.

Table 2 Physical properties for numerical calculation.

	Water	Ethanol	Rubber
ρ [kg/m³]	998	785	1415
c [m/s]	1498	1207	1030
β [-]	3.5	6.2	-
α [Np/m]	$25.3 \times 10^{-15} f^2$	$52.3 \times 10^{-15} f^2$	-
κ [W/(m K)]	0.602	0.168	-
μ [Pa s]	1.004×10^3	1.074×10^3	-
η_B [Pa s]	2.925×10^3	1.4×10^3	-

4. Numerical method

Figure 16 shows the computational domain for parametric sound propagation through different fluid layers in water, which is set to 500×250 mm in axial and radial directions, respectively. For the parametric sound propagation through different fluid layers, the computational domain includes the different fluid (ethanol) domain: Ω_D and two water domains: Ω_{W1} and Ω_{W2} with the input boundary z_{in} for water/different fluid interface and output boundary z_{out} for different fluid/water interface. For the sound pressure calculation in Ω_{W1}, the sound source on $z = 0$ is used as an initial condition prescribed by two different primary frequencies as follows:

$$S = p_0(sin2\pi f_1 t + sin2\pi f_2 t)$$
Equation 47

where $f_1 (= f_C - f_D)$ and $f_2 (= f_C + f_D)$ are the two primary frequencies, f_C and f_D are the center and difference frequencies of the primary waves, respectively, and t is time. The initial sound source distribution in radial direction is shown in Fig 17.

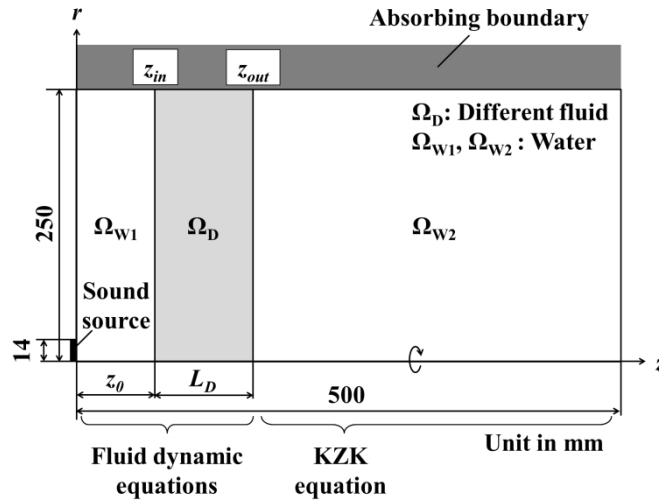Figure 16 Computational condition of sound propagation through different fluid layers for hybrid model.
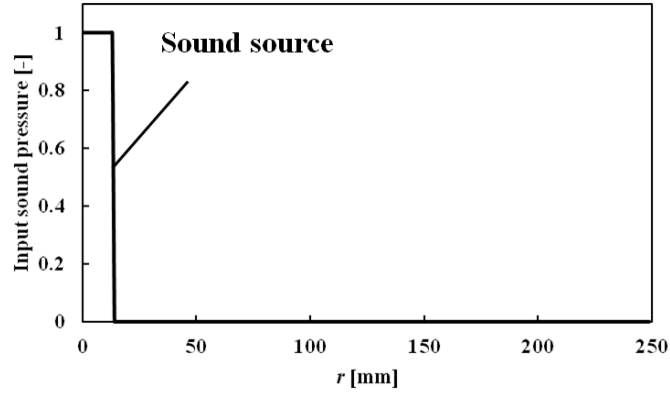
Figure 17 Distribution of sound source in radial direction. Note that sound pressure is normalized by input sound pressure.

As mentioned in Section 4.2.2, the KZK equation is limited to one-way nonlinear sound propagation although it is accurate enough for most application in underwater acoustic with low numerical cost. However, the difference in the acoustic impedance Z between two fluids causes reflection and refraction at the interface of two fluids, which generates an amplitude loss in forward propagating acoustic waves. In order to consider such phenomena at the water/different fluid and different fluid/water interfaces during sound propagation, the sound pressures in Ω_{W1}, Ω_D and the sound pressures on z_{out} in Ω_{W2} are calculated using the fluid dynamic equations with the absorbing boundary as shown in Fig 18. Then, the distribution of sound pressure on z_{out} in Ω_{W2} is transferred to the KZK equation as an initial condition to consider the reflection loss at water/ethanol and ethanol/water interfaces during sound propagation. It should be mentioned that the fluid dynamic model in the near field is solved in time domain, while the KZK equation in the far field is solved in frequency domain. To smoothly connect the sound pressure at the interface, the sound pressure distribution on z_{out} in Ω_{W2} as the initial condition of KZK equation is prescribed by Fourier coefficients: h, g of sound pressure evaluated from the sound pressure on z_{out} in Ω_{W2} obtained by solving the fluid dynamic equations. Therefore, the sound pressure distributions in the fluid dynamic equations are not affected by the results obtained from the KZK

32

4. Numerical method

equation in the hybrid model. Note that the computational cost in the hybrid model increases with increasing length of the different fluid layer due to the large computational cost in solving the fluid dynamic equations.

The computational domain in the KZK equation is also surrounded by the absorbing boundary to minimize acoustic reflections from the end of the computational domain in radial direction. The governing equation for absorbing boundary is defined as follows,

$$\frac{\partial^2 p*}{\partial \tau * \partial \sigma} - \underline{MR_d \frac{\partial^2 p*}{\partial \tau *^2}} - \frac{1}{2\sigma_D}\frac{\partial^2 p*^2}{\partial \tau *^2} - \frac{1}{4}\nabla_\perp^2 p* = 0 \quad \text{Equation 48}$$

where M is the artificial absorption coefficient for the KZK equation. Note that the absorbing term is underlined in Equation 48. And the artificial absorption coefficient in KZK equation can be defined as

$$M = \alpha\{1 + M_{max}(L_i / L_{AB})\} \qquad \text{Equation 49}$$

where M_{max} is the maximum of the artificial absorption coefficient. In this paper, $M_{max} = 200$ is used.
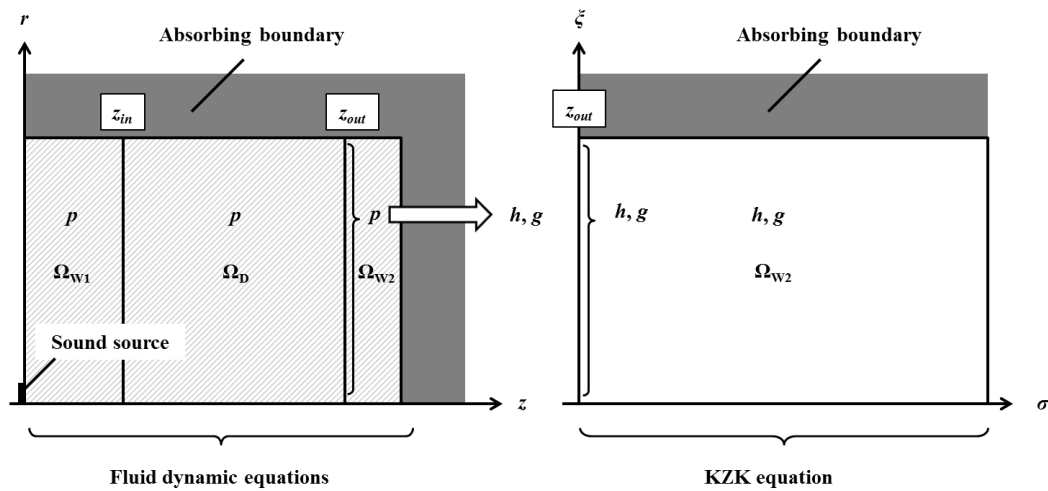

Figure 18 Schematic description of interface calculation in hybrid model.

4.3 Grid resolution

The hybrid model is applied to the parametric sound propagation emitted from a sound source of 14 mm in radius in water, where the two different primary frequencies were set to $f_1 = 1.1$ MHz and $f_2 = 1.2$ MHz to generate a difference frequency of $f_D = 0.1$ MHz and a sum frequency of $f_S = 2.3$ MHz. The input sound pressure was $p_0 = 50$ kPa.

Figure 19 shows the variation of sound pressure at $z = 200$ mm on beam axis with grid resolution using the fluid dynamic equations and the KZK equation. The material properties used in the numerical simulation are summarized in Table 2. Note that the grid sizes in numerical simulation are set to $\Delta = 1/\lambda_R$, where λ_R is the number of grid per wavelength of primary frequency. The results show that the numerical results in the KZK equation are saturated around $\lambda_R = 20$, while those are saturated around $\lambda_R = 50$ in the fluid dynamic equations. And the numerical results did not change with increasing of the grid number per wavelength.

Figure 20 shows the variation of sound pressure at $z = 200$ mm on beam axis from the sound source with various interface positions with grid size of $\lambda_R = 50$ in the hybrid model. The results showed that the variation of interface position has small influence on the numerical results in the hybrid model. From these results, the grid size in hybrid model is set to $\lambda/50$ and the interface is located at the different fluid/water interface to consider the reflection at the two different fluid boundaries in this paper. Note that the comparisons of the numerical results of hybrid model with that of the KZK equation are shown in Appendix B.
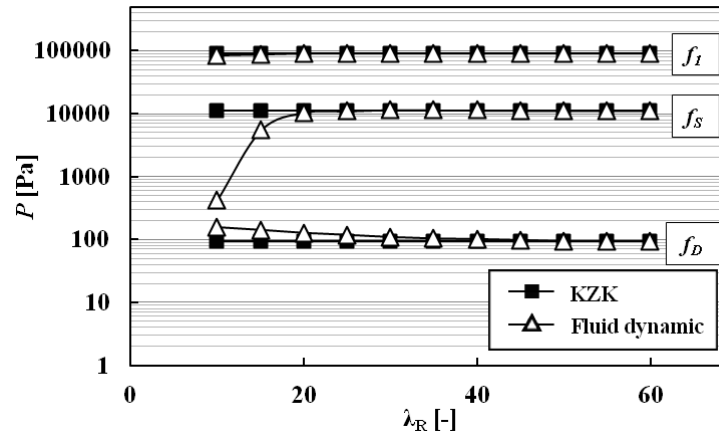
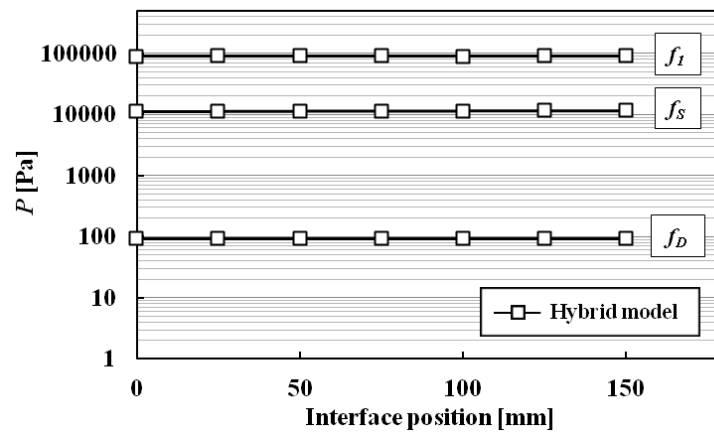Figure 19 Variation of sound pressure with grid resolution.

Figure 20 Variation of sound pressure with interface position.

5. Results and discussion

5.1 Sound distribution

In order to predict sound distribution of the parametric sound at the sum and difference frequencies through the different fluid layers, both the numerical simulation and experiments were carried out for nonlinear sound propagation from a circular sound source prescribed by Equation 47, where the two different primary frequencies were set to $f_1 = 1.1$ MHz and $f_2 = 1.2$ MHz to generate a difference frequency of $f_D = 0.1$ MHz and a sum frequency of $f_S = 2.3$ MHz, which is illustrated in Fig 16. The input sound pressure was $p_0 = 50$ kPa. The transmittance time of the sound source signal was 80 μs, this gave a quasi-continuous sound pressure field.

The different fluid layer was placed at a distance of $z_0 = 70$ mm away from the transducer in the water tank and the sound waves were measured by traversing the hydrophone using a three-dimensional positioning stage as described in Section 3. A circular cylinder with a $R_C = 120$ mm radius with a thin rubber film of thickness 0.1 mm contained ethanol to prevent any mixing of ethanol and water. The length of the different fluid (ethanol) layer varied as $L_D = 70, 100,$ and 150 mm. In this experiment, a circular type transducer of 14 mm in radius with a flat surface was used as a sound source. The emitted sound propagated through the different fluid layer and was received by two different hydrophones in the water tank. A hydrophone with uniform sensitivity in the frequency interval of 1 to 3 MHz was used for the sum frequency measurements, and a hydrophone with uniform sensitivity in the frequency range below 0.5 MHz was used for the difference frequency measurement. The acoustic parameters used in numerical studies are listed in Table 2. Note that in the numerical simulation, the absorption coefficient in liquid is assumed to be proportional to the square of

5. Results and discussion

the frequency in the fluid [50].

Figure 21 shows the numerical results of the sound pressure distribution at the primary frequency f_1 = 1.1 MHz with and without the different fluid layer as a contour map. The distribution of sound pressure with and without the different fluid layer show extensive fluctuations near the sound source due to the wave interferences of the primary wave. This is also referred to as 'diffraction effect'. However, the sound pressure in the different fluid layer was smaller than that in water due to the smaller acoustic impedance of ethanol. It was also found that the sound pressure distribution after the different fluid layer was similar to that in water without the different fluid layer. The maximum sound pressure was $p_{\max}$ = 91.8 kPa through the different fluid layer less than $p_{\max}$ = 99.3 kPa in water. This is due to the reflection loss through the different fluid layer.

Figure 22 shows the sound pressure distribution at the difference frequency f_D = 0.1 MHz with and without the different fluid layer as a contour map. The sound pressure at the difference frequency, with or without the different fluid layer, gradually increases without any fluctuation in the near field due to the accumulation of nonlinear effect during sound propagation. At the same time, the sound pressure at the difference frequency generated in the different fluid layer was larger than that in water due to the large nonlinear property of ethanol. The maximum sound pressure at the difference frequency is p_{max} = 0.32 kPa at the different fluid/water interface with z = 170 mm away from sound source through different fluid layer exhibiting a sharp peak. On the other hand, in the water, the maximum sound pressure was found to be p_{max} = 0.096 kPa at z = 250 mm.

Figure 23 shows the sound pressure distribution at the sum frequency f_S = 2.3 MHz with and without the different fluid layer as a contour map. The results show that the sound pressure at the sum frequency gradually increases in the near field and it continues in the far field due to accumulation of nonlinear effects

37

during sound propagation generated by the combination of the smaller diffraction effect of sound pressure at the sum frequency than primary one. This behavior was also observed at the difference frequency. There are no clear peaks in the sound pressure, while the maximum sound pressure at the sum frequency through different fluid layer was found to be p_{max} = 27.3 kPa at z = 232 mm with the different fluid layer. This value is larger than p_{max} = 13.0 kPa at z = 300 mm in water. It was also found that the amplitude of the sum frequency is much larger than that of the difference frequency. This is because the conversion efficiency from the primary waves increases with increasing secondary wave frequency. Note the abrupt increase of the sound pressure at primary, sum and difference frequencies at the different fluid layer/water interface at z = 170 mm away from the sound source is due to the larger acoustic impedance of water than that of ethanol [51].
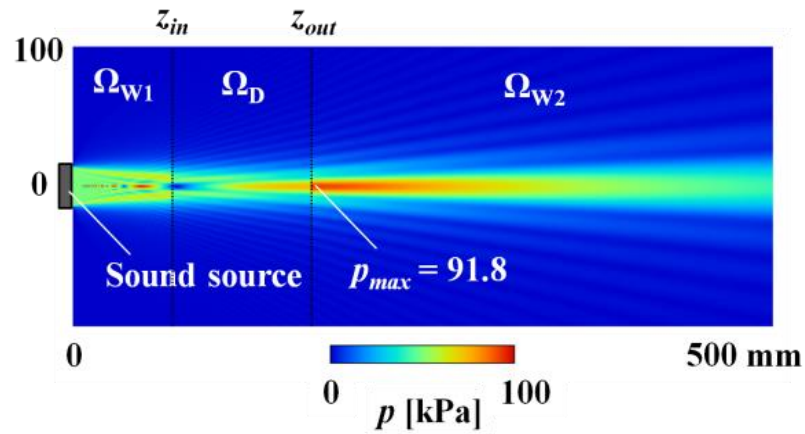
a: with etahnol layer
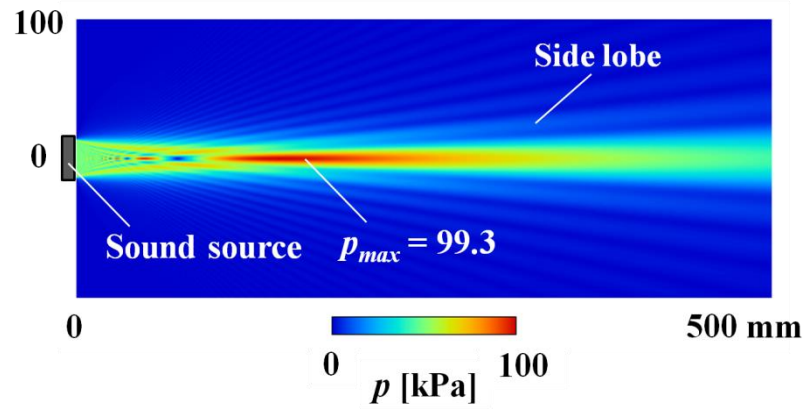
b: without ethanol layer

Figure 21 Sound pressure distribution of primary frequency.

5. Results and discussion
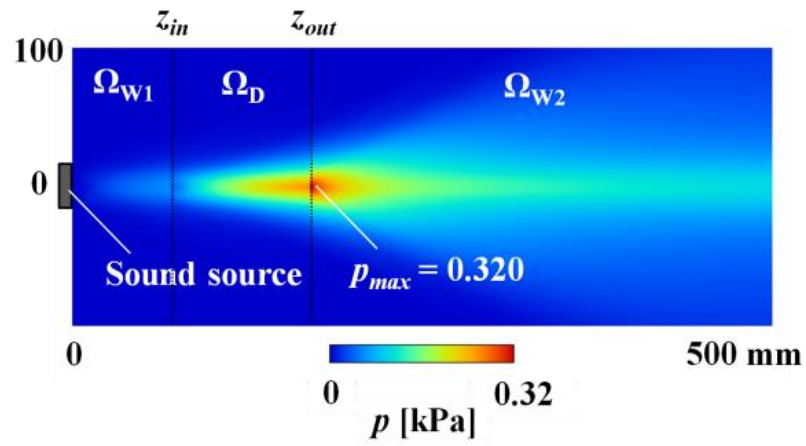
a: with etahnol layer
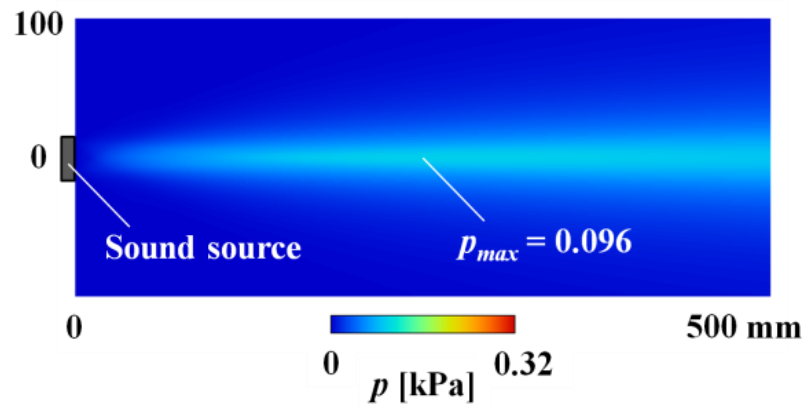
b: without ethanol layer

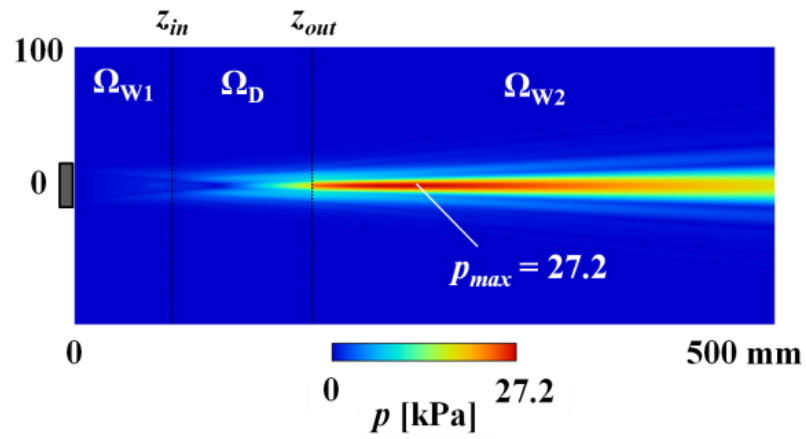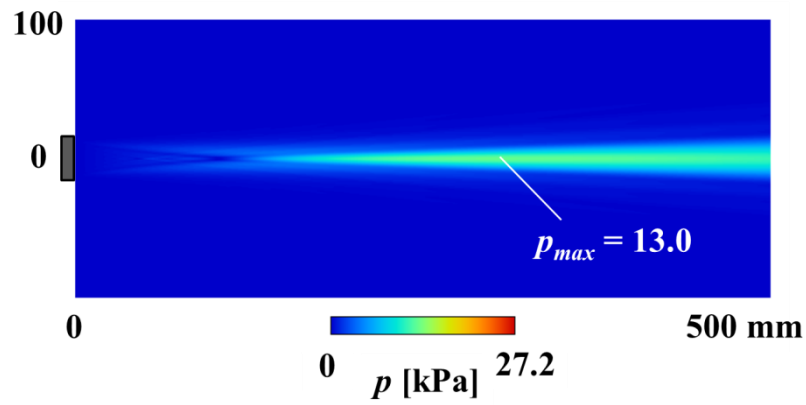Figure 22 Sound pressure distribution for the difference frequency.

5. Results and discussion

a: with etahnol layer

b: without ethanol layer

Figure 23 Sound pressure distribution for the sum frequency.

5. Results and discussion

In order to understand the effect of ethanol layer on radial distribution of sound pressure at sum and difference frequency, the beam directivity is evaluated using sound pressure distribution perpendicular to the beam axis obtained at $z = 250$ mm away from the sound source. Note that each sound pressure distribution is normalized by their maximum sound pressure. Figure 24 shows the radial sound pressure distribution at primary frequency $f_1 = 1.1$ MHz perpendicular to the beam axis obtained at $z = 250$ mm away from the sound source. The results show that the side lobes were observed due to the interferences of the primary wave during sound propagation which was the same phenomena described as 'diffraction effect' in Fig 21. However, they gradually decrease with increasing radial distance. On the other hand, there was no significant difference between the sound pressure distributions through different fluid layer and that in water.

Figure 25 shows the radial sound pressure distribution at the difference frequency $f_D = 0.1$ MHz perpendicular to the beam axis at $z = 250$ mm away from the sound source. The results show that the sound pressure increases with the different fluid layer length. In contrast to the primary frequency, side lobes were not observed with or without the different fluid layer. It is also found that the beam directivity decreases through ethanol layer due to the narrower distribution of the difference frequency at the ethanol/water interface generated by the higher directivity of the difference frequency in ethanol layer compared to that in water.

Figure 26 shows the radial sound pressure distribution at the sum frequency $f_S = 2.3$ MHz perpendicular to the beam axis at $z = 250$ mm away from the sound source. The results show that the sound pressure at the sum frequency increases with increasing length of the different fluid layer. This was also observed in the radial sound pressure distribution at the difference frequency. In contrast to the difference frequency, side lobe observed had small amplitude though it was much smaller than that at the primary frequency.

5. Results and discussion
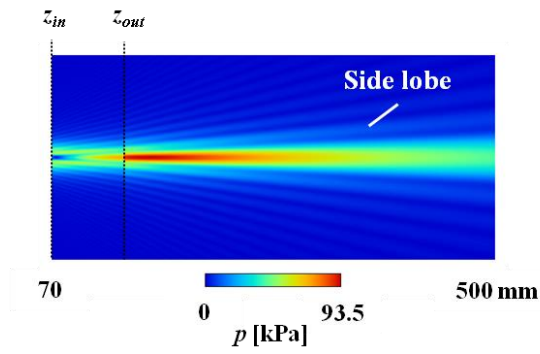
(a) $L_D = 70$ mm
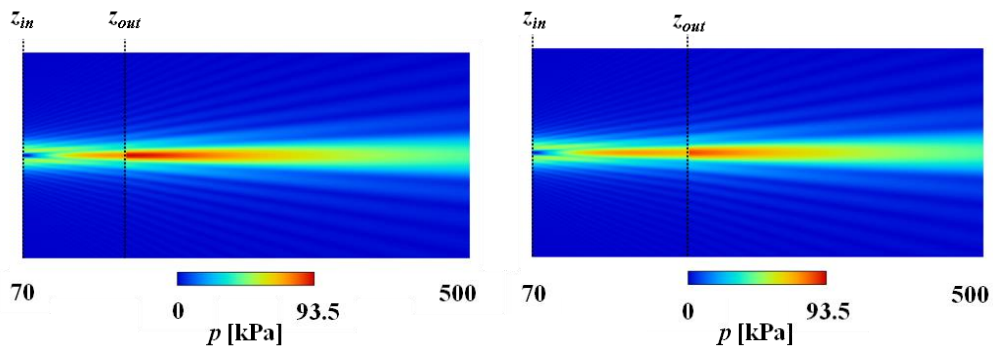
(b) $L_D = 100$ mm　　　　　　(c) $L_D = 150$ mm

(d) Beam directivity

Figure 24 Acoustic beam characteristic of primary frequency with and without different fluid layer at $z = 250$ mm distant from sound source.

(a) L_D = 70 mm

(b) L_D = 100 mm   (c) L_D = 150 mm
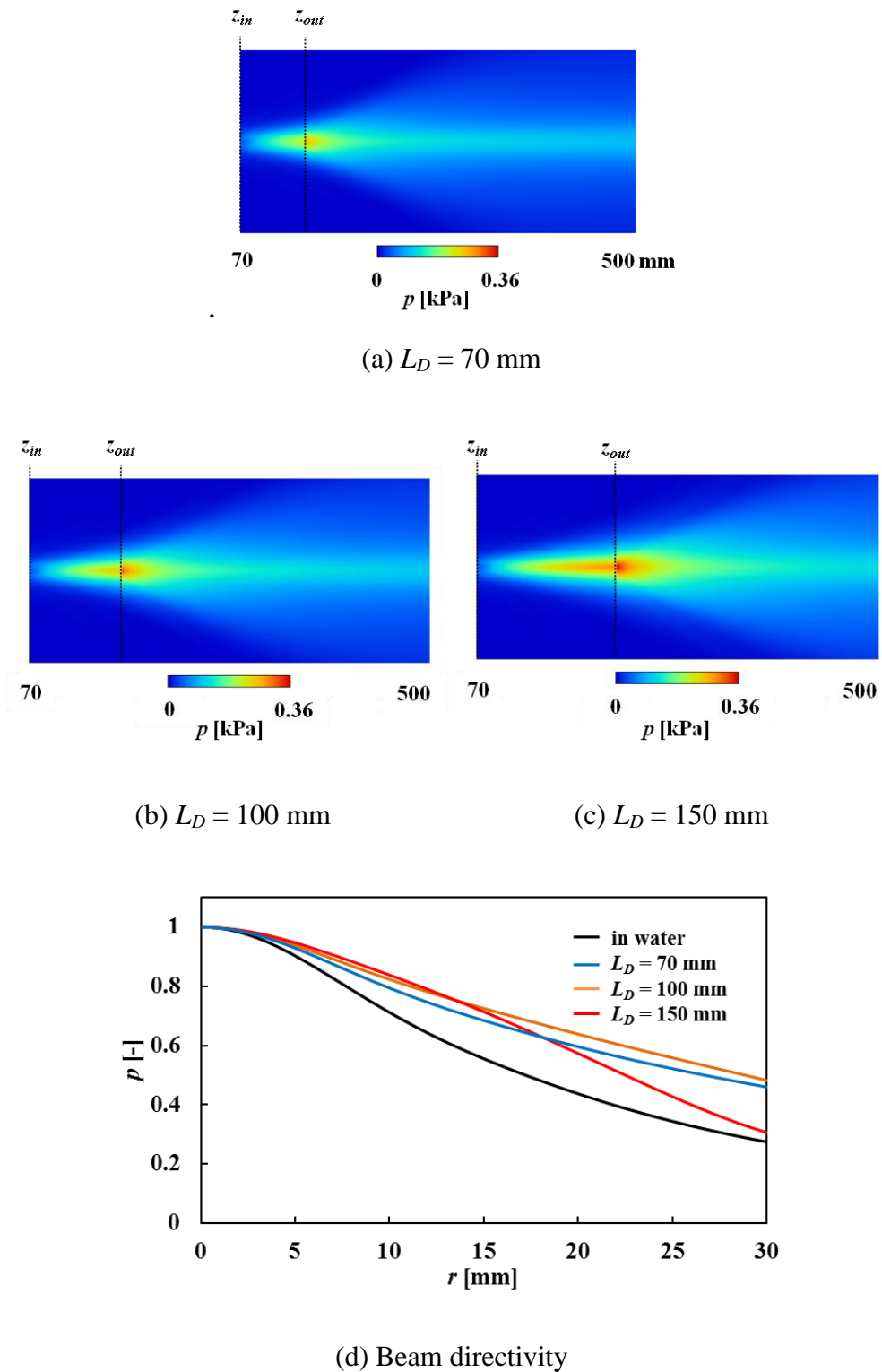
(d) Beam directivity

Figure 25 Acoustic beam characteristic of difference frequency with and without different fluid layer detected at z = 250 mm away from sound source.

5. Results and discussion
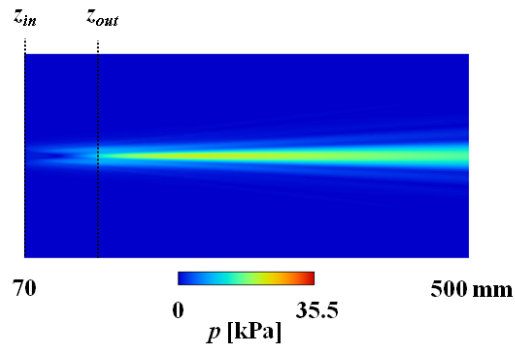
(a) $L_D = 70$ mm
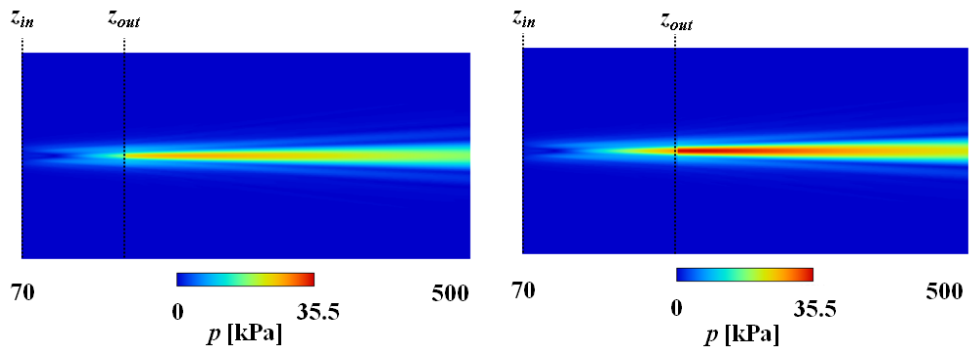
(b) $L_D = 100$ mm

(c) $L_D = 150$ mm
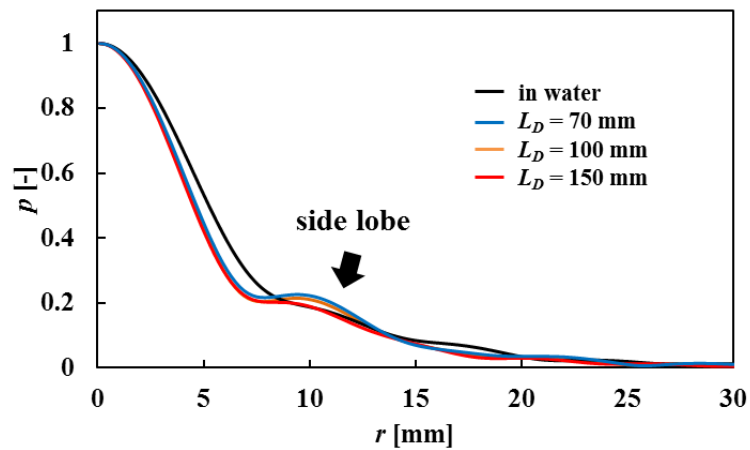
(d) Beam directivity

Figure 26 Acoustic beam characteristic of sum frequency with and without different fluid layer detected at $z = 250$ mm away from sound source.
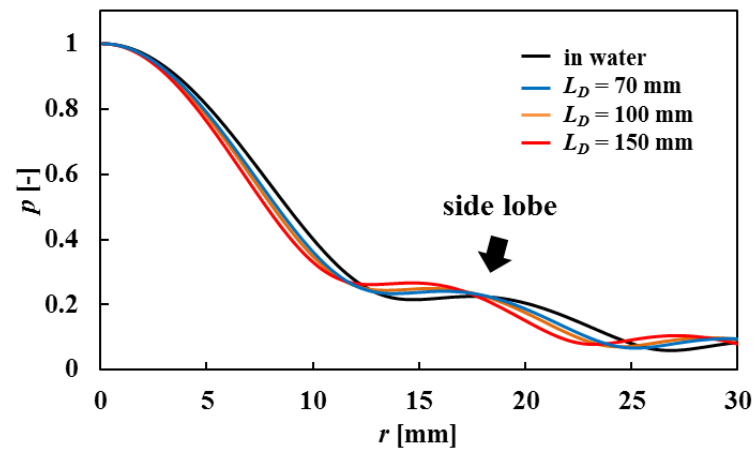
5. Results and discussion

Figures 27 and 28 show the acoustic beam characteristic of sum and difference frequencies perpendicular to the beam axis obtained at $z = 140$ mm away from sound source in different fluid layer comparing with those in water. Note that each sound pressure distribution is normalized by their maximum sound pressure. Solid and dash lines indicate the numerical results with and without different fluid layer, respectively. The results show higher directivity of difference frequency in different fluid than that in water at the same distance from the sound source due to the small diffraction effect in ethanol than that in water. On the other hand, the acoustic beam characteristic of sum frequency does not show clear difference in beam directivity between the acoustic beam characteristic through different fluid layer and that in water, because diffraction effect largely affect for low frequency wave than high frequency wave. Therefore, large enhancement of difference frequency was affected by both nonlinear fluid property of ethanol but also small diffraction effect in different fluid layer, that results in larger enhancement of difference frequency and its peak at different fluid/water interfaces which was not observed in sum frequency.
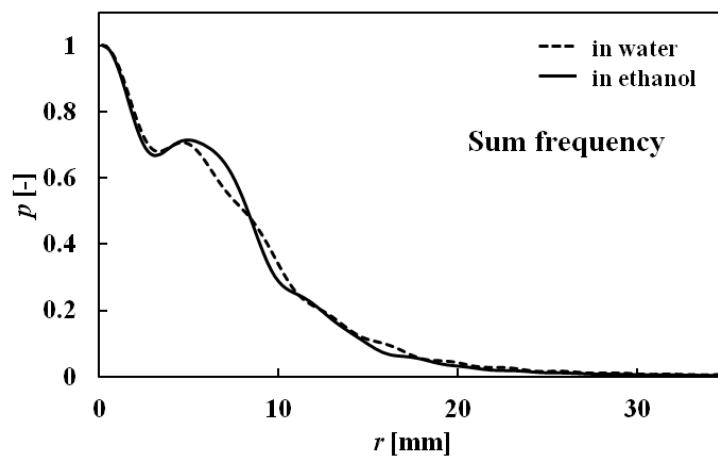
Figure 27 Acoustic beam characteristics of parametric sound at the sum frequency in different fluid layer at $z = 140$ mm away from sound source.
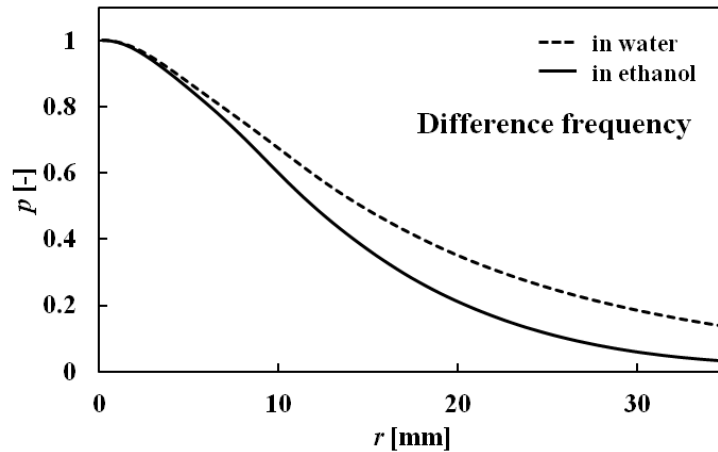
Figure 28 Acoustic beam characteristics of parametric sound at the difference frequency in different fluid layer at $z = 140$ mm away from sound source.

5.2 Enhancement ratio

Enhancement ratio for the sum and difference frequencies through different fluid layers were evaluated numerically and experimentally. For comparative purposes, the theoretical calculation based on the Burgers equation was carried out. Note that the enhancement ratio in the theoretical calculation is not affected by the frequency of the parametric sound because both diffraction and absorption effects are neglected in the theoretical calculation. Therefore, the enhancement ratios at the sum and difference frequencies are of the same value in the theoretical result.

Figure 29 shows the enhancement ratio at the difference frequency for the three different fluid layer lengths. The results show that η at the difference frequency gradually increases in the different fluid layer due to the larger nonlinearity of ethanol than that of water during sound propagation. Then, η increases rapidly at the different fluid/water interface, due to the larger acoustic impedance of water compared to ethanol. Both numerical and theoretical results show the similar tendency of increasing η with increasing z in the different fluid layer and decreasing η with increasing z in the far field. The maximum

5. Results and discussion

enhancement ratio was 3.7 at an ethanol length of 150 mm. However, there is a tendency for η in both the numerical simulation and the experiment to be larger than that from the theoretical calculation in the vicinity of the different fluid/water interface. This is due to the smaller diffraction effect in ethanol than in water. In addition, there is a tendency that experimental results have a larger value than the numerical results. This discrepancy may be explained by an existing accumulation of nonlinear effect in rubber. Such an effect is not considered in the numerical calculation and may account for the smaller amplitude at the difference frequency in second water layer.

Figure 30 shows the enhancement ratio at the sum frequency for the three different lengths of the different fluid layer. As in the case of the difference frequency, the results showed that η increases with increasing axial distance in the different fluid layer and η decreases with increasing axial distance in the far field. The maximum enhancement ratio was 2.7 at an ethanol length of 150 mm which was smaller than that of difference frequency which can be attributed to the diffraction effect in the different fluid layer. The increase of η at the sum frequency in the different fluid layer was smaller than that at the difference frequency in the same domain. This is due to the diffraction effect in the different fluid layer as it is described in Section. 5.1 above. It was also found that the large dip and peak of η at the sum frequency around $z = 100$ mm in the different fluid layer is due to the diffraction effect of the sum frequency in the near field. This behavior was not in the theoretical results because the diffraction effect is neglected in the theoretical model.

Figures 31 and 32 show the numerical results for the maximum enhancement ratio η_{max} at the sum and difference frequencies with respect to the length of the different fluid layer L_D for the three different layer positions z_0 from the sound source. The two primary frequencies were set to $f_1 = 1.1$ MHz and $f_2 = 1.2$ MHz. The results indicate that η_{max} increases with increasing length of the

different fluid layer and it is largest when the different fluid layer is close to the sound source. This is where a large accumulation of nonlinear acoustic effects is caused. Further, η_{max} tends to be saturated for long lengths of the different fluid layer. It is also found that η_{max} at the difference frequency is larger than that at the sum frequency due to the diffraction effect which was described in Section 5.1. Note that numerical results for short lengths of the different fluid layer were not attained except for $L_D = 0$. This is due to the difficulty in obtaining steady state results due to the interaction, in this range, of the forward propagating wave with the reverberation wave.

Figure 29 Enhancement ratio for difference frequency along axial distance. Marks, solid lines and dot lines denote the enhancement ratio using experimental results, numerical results and theoretical results.
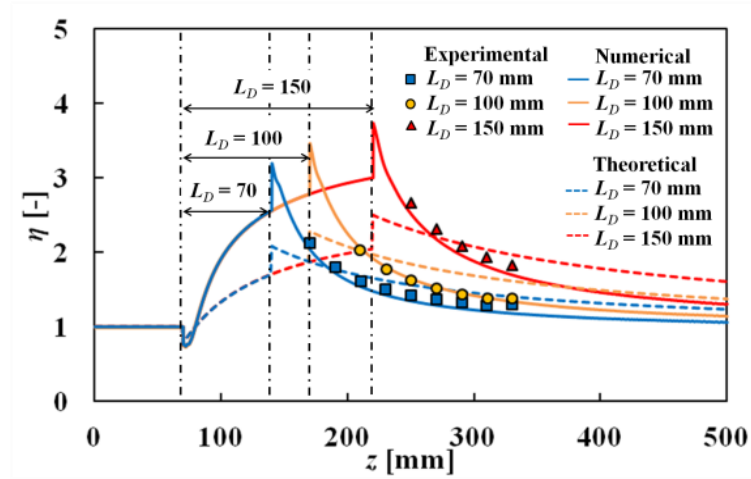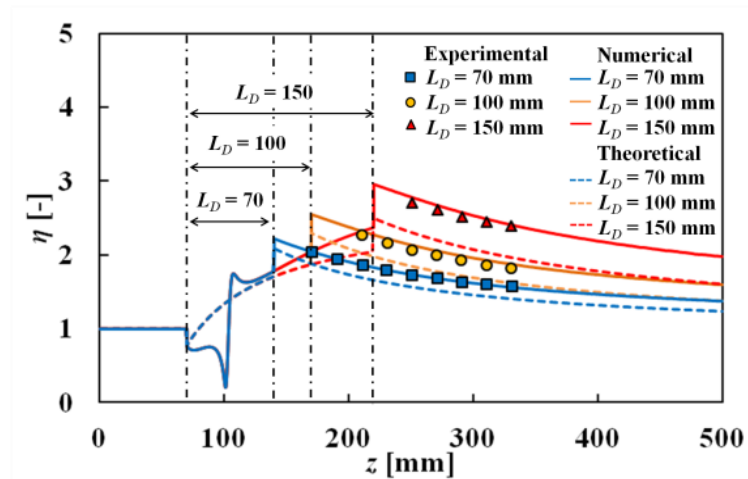

Figure 30 Enhancement ratio for sum frequency along axial distance. Marks, solid lines and dot lines denote the enhancement ratio using experimental results, numerical results and theoretical.
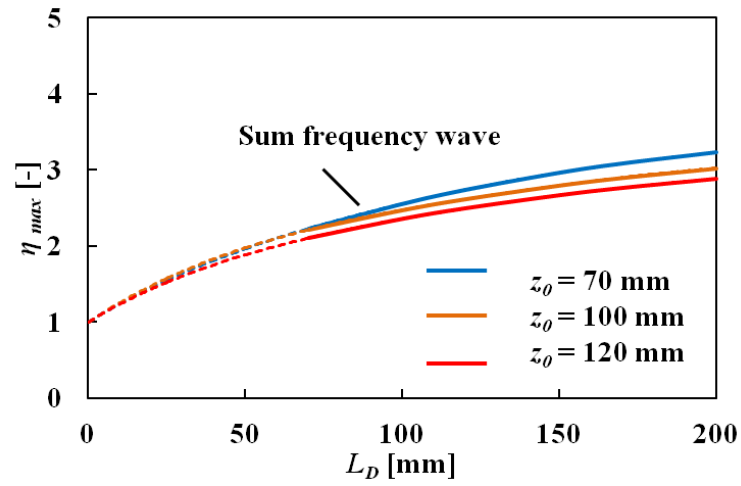
Figure 31 Variation of η_{max} with L_D. (sum frequency)
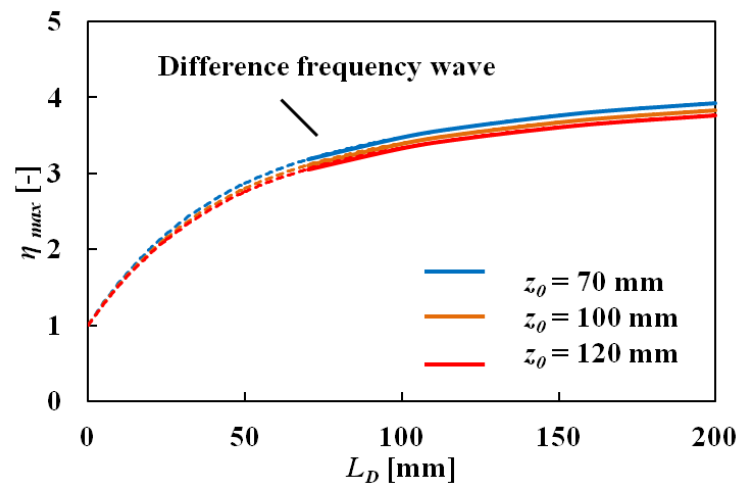
Figure 32 Variation of η_{max} with L_D. (difference frequency)

5.3 Nonlinear effects

In order to understand the nonlinear effects in water layer: Ω_{W2}, the numerical calculation is carried out for the sound propagation with and without nonlinear term in Ω_{W2}. The nonlinear effect is evaluated by the difference of the sound pressure for the parametric sound at the sum and difference frequencies for linear and nonlinear cases: $p_N - p_L$. p_N is the sound pressure of the parametric sound at sum and difference frequencies and primary wave calculated using nonlinear term in the governing equation and p_L is the sound pressure at the sum and difference frequency without nonlinear term in the governing equation. For comparative purposes, the nonlinear effect at the primary frequency is also evaluated. The ethanol layer is set at $z_0 = 70$ mm and the same initial condition on z_{out} considering the nonlinear effect in both Ω_{W1} and Ω_D is used for both linear and nonlinear cases. Note that the other computational conditions are the same as that used in Section 5.1.

Figures 33 and 34 show the variation of nonlinear effect in water layer along beam axis at the sum and difference frequency, respectively. The results indicate that the nonlinear effect of parametric sound at sum and difference frequency gradually increase with increasing of propagation distance, while it saturated around 300 mm due to the decreasing of the sound pressure at primary frequency in the far field which is described in Section 5.1. It is also found that the nonlinear effect in the parametric sound at the sum and difference frequencies increase with decreasing of the ethanol layer length due to the small conversion of primary frequency to the secondary waves in ethanol layer. On the other hand, the nonlinear effect in primary frequency decreases with increasing of propagation distance due to the energy conversion of primary frequency to the sum and difference frequencies.
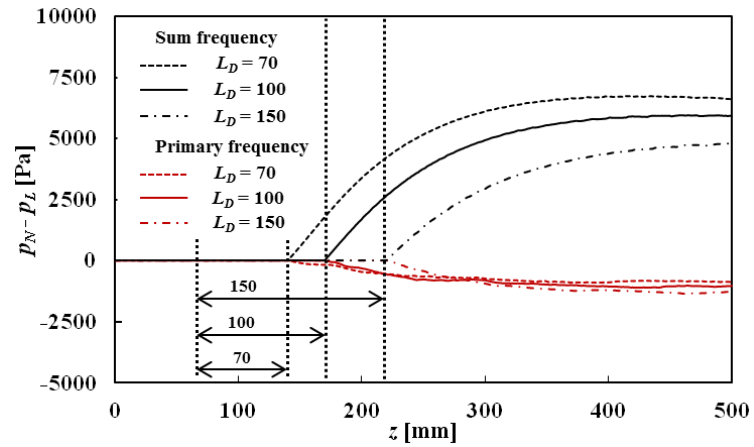
Figure 33 Variation of nonlinear effect in water layer. (sum and primary frequency)
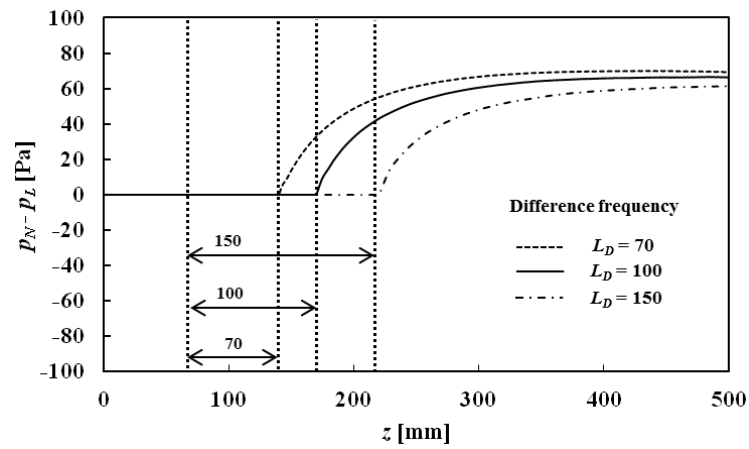
Figure 34 Variation of nonlinear effect in water layer. (difference frequency)

6. Application

The parametric sound enhancement technique with the different fluid layers is applied to the noninvasive measurement of a square cylinder in water together with a shadow method [3, 36, 51]. First, the nonlinear shadow method that utilizes the parametric sound is described, then, nonlinear shadow method combined with the parametric sound enhancement technique with the different fluid layers is studied.

6.1 Shadow method

Shadow method is an efficient ultrasound imaging technique for diagnosis of inner and outer state for target object, which utilizes acoustic shadow of the object backward. The shadow occurs at the area where acoustic signal intensity is lower than other area due to the high acoustic impedance differences at the medium interface of the target. It has higher signal intensity than acoustic images obtained by pulse echo method because of low attenuation during sound propagation in medium material. It is also known that the shadow method can be applied to rough surface that causes the acoustic scattering where the target detection using pulse echo method is difficult to apply for the limitation of critical angle of reflection to the target [52 - 55]. For these better acoustic characteristics, it has been applied to a detection of flaw defects and a characterization of materials [56 - 58]. However reverberation artifact repeatedly occurred in the measurement due to the acoustic impedance difference between the target and water, especially when transducer and hydrophone receiver are located vertical to the surface of the target and it causes virtual image of the target material [59]. In order to reduce the reverberation artifact in acoustic shadow imaging, the sound pressure of the transmitter can be reduced or the transducer can be inclined to the target surface, while the signal amplitude of imaging is reduced and causes lower

6. Application

SNR (signal to noise ratio) in acoustic shadow imaging. Therefore, the reducing reverberation artifact is an important topic in the application to underwater measurement and material characterization in comparison with the medical application due to higher environmental and machinery noise. Furthermore, it is difficult to estimate the incident angle of the beam to the target in the underwater measurement.

Parametric sound generation is a promising method to reduce reverberation artifact of acoustic shadow imaging in water. When two different frequency of sound waves (primary waves) are transmitted in the same direction, the secondary wave such as sum and difference frequencies are generated by nonlinear interaction of finite amplitude waves for its acoustic characteristic such as high directivity with low side lobe beam, which has been described in Section 1 and 5.

The experiments were carried out for acoustic shadow imaging of square cylinder made of aluminum, which is summarized in Fig 35 (a), (b). The water tank was 600 mm long and 500 mm wide with 500 mm deep, and the water temperature was maintained at 298 K by temperature control unit. Both the transducer and hydrophone used in the experiment were circular type with flat surface. The size of the transducer was 12 mm in diameter and that of the hydrophone was 6 mm in diameter. It should be mentioned that hydrophone potentially has space averaging error in measurement, and such error may be reduced by smaller size of the hydrophone. However smaller size hydrophone also reduces the sensitivity and has difficulty in measuring the secondary waves which has lower signal level than that of the primary waves. The center point of the square cylinder was located at the axial position $z = 85$ mm from the transducer in water and the hydrophone was located at $z = 200$ mm from the transducer on beam axis.

6. Application

The transducer and hydrophone were traversed in the same direction across the square cylinder and the hydrophone was set (a) vertical to the square cylinder and (b) 45 degree to square cylinder, which allows the detection of the acoustic signal from the transducer influenced by the presence of the square cylinder and reconstructs two-dimensional acoustic image as shown in Fig 36 (a), (b). The sampling of the acoustic signal was carried out by traversing the transducer and hydrophone for every 1 mm across the target by three-dimensional positioning stage. Then, the two-dimensional shadow images were reconstructed after detecting the envelope of each wave by Hilbert transformation [60 - 62].

The transducer was excited by two different frequencies of primary waves and the driving signal s is written by the following equation,

$$s = s_0 \left(\sin 2\pi f_1 t + \sin \left(2\pi f_2 t + \pi \right) \right) \ \left(0 < t < tr \right) \qquad \text{Equation 50}$$

where s_0 is the signal amplitude of primary waves and t is a time. The two frequency of primary waves were set f_1 = 2 MHz and f_2 = 2.4 MHz with transmittance time of tr = 2.5 μs. The signal was observed by the digital storage oscilloscope, where the spurious reflections were eliminated using the time gate, and the received signal was averaged over 64 times at each position to minimize the white noise in this measurement. The sound pressure was measured using the receiver hydrophone which had flat frequency response over the frequency range from 2 MHz to 8 MHz. Note that the initial time of signals recorded by hydrophone is set as a time when acoustic wave is transmitted from transducer.

6. Application
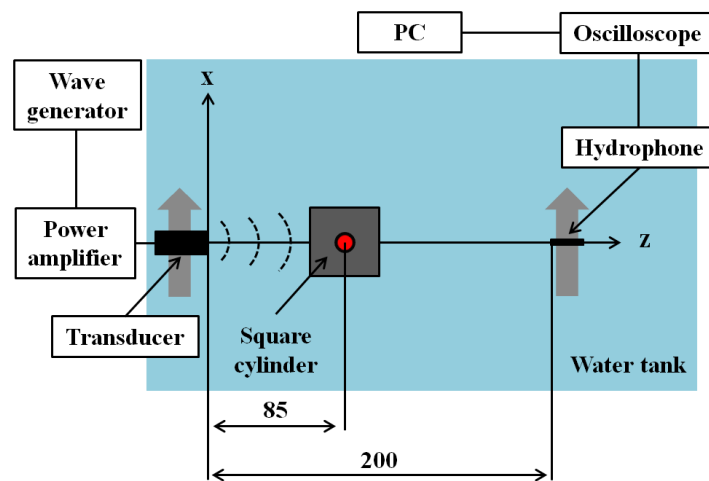
(a) Top view of experimental setup
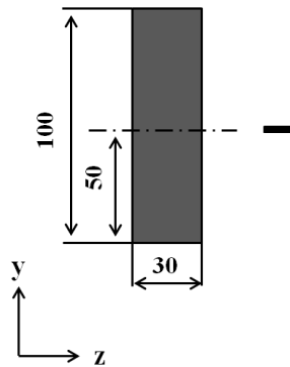
(b) Side view of square cylinder

Figure 35 Noninvasive detection of square cylinder in water. (unit in mm)
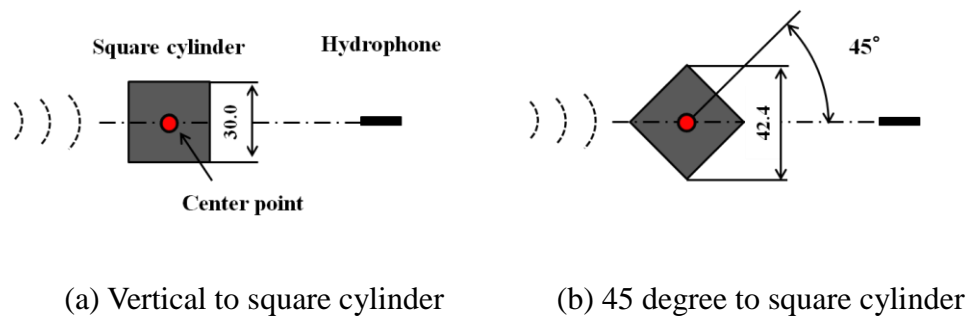
(a) Vertical to square cylinder

(b) 45 degree to square cylinder

Figure 36 Arrangement of square cylinder and hydrophone. (unit in mm)

6.2 Nonlinear sound propagation through square cylinder

Figures 37 (a), (b) show the frequency spectrum of the sound signal detected by the hydrophone located at z = 200 mm with and without square cylinder, respectively. The center of the square cylinder is on the beam axis and the hydrophone is set behind the square cylinder, which is the vertical case in Fig 36 (a). The same input voltage was applied to the transducer in both cases and the frequency spectrum of the sound wave was evaluated using discrete Fourier transform, and the frequency spectrum is normalized by each maximum amplitude of the signal. Note that the signal level of the primary waves are reduced to 1/5 by the influence of the square cylinder (36.7 mV without square cylinder → 7.01 mV with square cylinder), while that of the secondary wave is reduced more strongly (8.88 mV without square cylinder → 0.81 mV with square cylinder). The results of the normalized pressure amplitude show the generation of secondary wave at the sum frequency (centered at f = 4.4 MHz) due to the nonlinear interaction of finite amplitude sound propagation. Furthermore, the pressure amplitude at higher harmonics (centered at f = 6.8 MHz) shows a similar trend as the secondary wave with and without square cylinder. These results indicate that acoustic shadow imaging using secondary wave can be applied to eliminate the small amplitude phenomena in imaging, such as the reverberation artifact in shadow method, when the secondary wave is properly amplified.
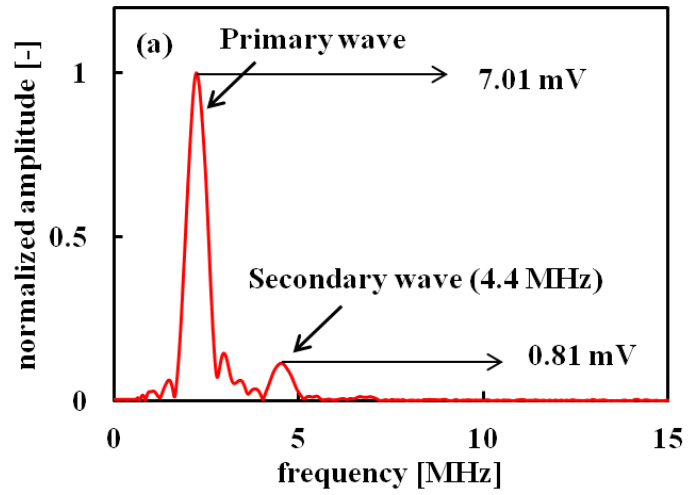
(a) With square cylinder
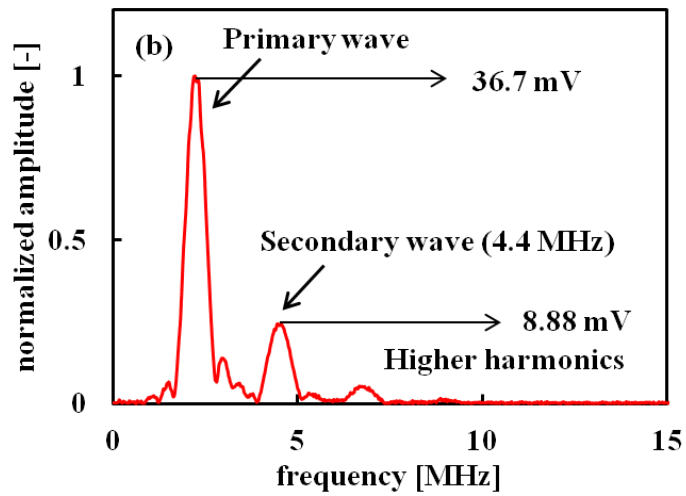
(b) Without square cylinder

Figure 37 Frequency spectrum of parametric sound detected at $z = 200$ mm.

6.3 Nonlinear shadow method

The noninvasive detection of the square cylinder using nonlinear shadow method that utilizes the generation of secondary wave in water is studied. For the comparative purposes, linear shadow imaging was carried out by removing secondary wave by low-path filter with the cut-off frequency 3.3 MHz. Note that the linear shadow imaging corresponds to the conventional shadow method that utilizes primary waves. These images were normalized by each maximum amplitude that corresponds to the direct wave.

Figure 38 (a) and (b) show the linear shadow images of two different arrangements of hydrophone to square cylinder, respectively. These are the cases of beam axis vertical to square cylinder (Fig 38 (a)) and 45 degree to square cylinder (Fig 38 (b)). There are three kinds of signal distributions, which are numbered in 1, 2 and 3 in Fig 38 (a). These are the penetration wave through square cylinder, reverberation waves inside the square cylinder and the direct waves, respectively, while Fig 38 (b) shows no reverberation artifact in shadow image due to large incident angle of the beam to the square cylinder.

Figure 39 (a) and (b) show the nonlinear shadow images of two different arrangements of square cylinder and hydrophone, respectively. These are vertical to square cylinder (Fig 39 (a)) and 45 degree to square cylinder (Fig 39 (b)). There is a tendency of nonlinear shadow image to have sharper outline compared to linear shadow image due to the shorter wave length of the secondary wave than that of the primary waves, which are commonly observed in these results. The signal level of penetration wave and reverberation wave are greatly suppressed in the image using nonlinear shadow method in Fig 39 (a) compared to that of linear shadow method shown in Fig 39 (a). This is true for the case of 45 degree to square cylinder in Fig 39 (b).

6. Application

In order to verify the size measurement accuracy of nonlinear shadow method, the error of measurement is introduced as follows,

$$\varepsilon = \left| L_s - L_0 \right|$$

where L_s and L_0 are the side lengths measured by shadow method and actual size, respectively. Note that the shadow is defined by 10% amplitude of the direct wave.

Figures 40 (a) and (b) illustrate the signal amplitude distributions along traversed direction of two different arrangements of hydrophone to square cylinder, respectively. These are the cases of vertical to square cylinder (Fig 40 (a)) and 45 degree to square cylinder (Fig 40 (b)). The error of measurement ε is 4.1 mm in nonlinear shadow method and it is 9.0 mm in linear shadow method of Fig 40 (a), while the ε is 4.0 mm in nonlinear case and it is 9.3 mm in linear case in Fig 40 (b). These results indicate that the image using nonlinear shadow method shows sharper distribution, and the error is almost half in the nonlinear shadow method compared to that of the linear shadow method. This is due to the smaller refraction effect and higher directivity of secondary wave propagation than that of the primary waves. It should be mentioned that the nonlinear shadow method offer better measurement accuracy by eliminating the reverberation artifacts in imaging.
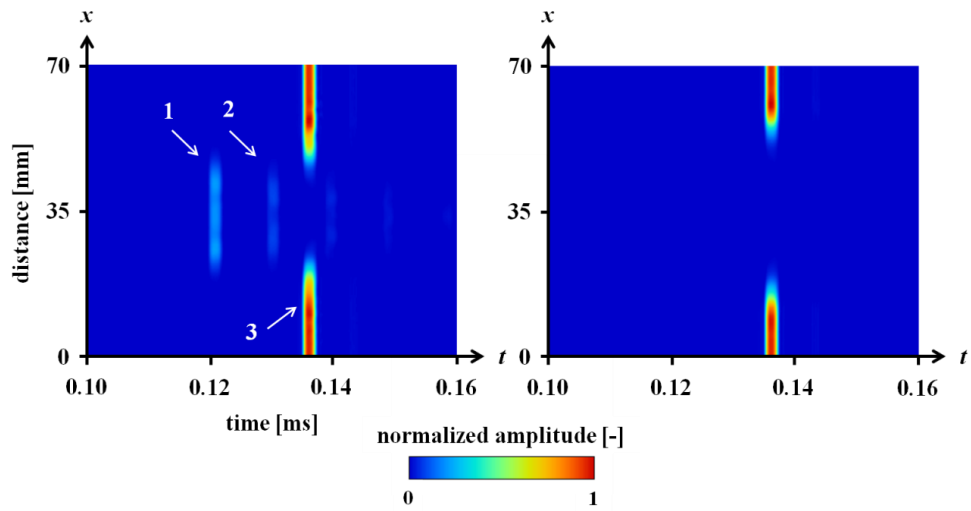
(a) Vertical to square cylinder   (b) 45 degree to square cylinder

Figure 38 Linear shadow image of square cylinder. (1: penetration wave, 2: reverberation wave, 3: direct wave)
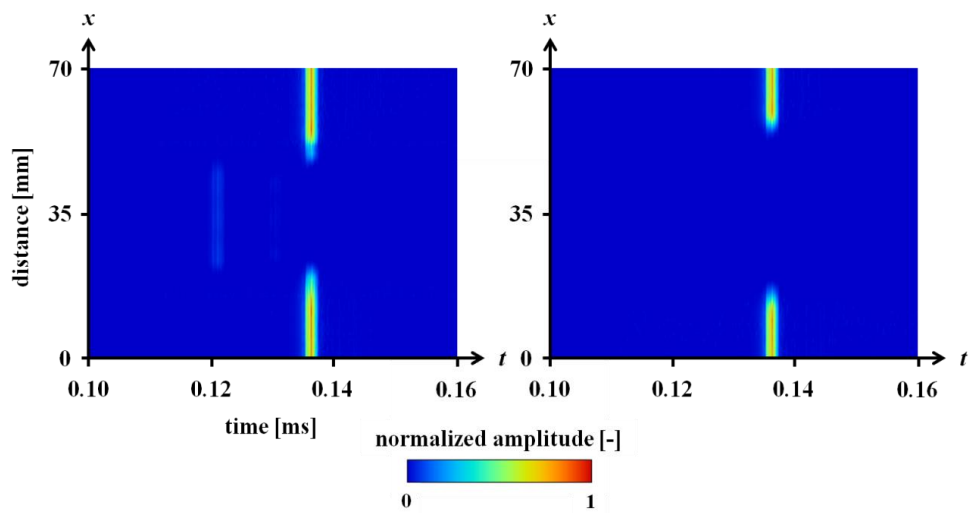
(a) Vertical to square cylinder   (b) 45 degree to square cylinder

Figure 39 Nonlinear shadow image of square cylinder.

(a) Vertical to square cylinder　　　(b) 45 degree to square cylinder
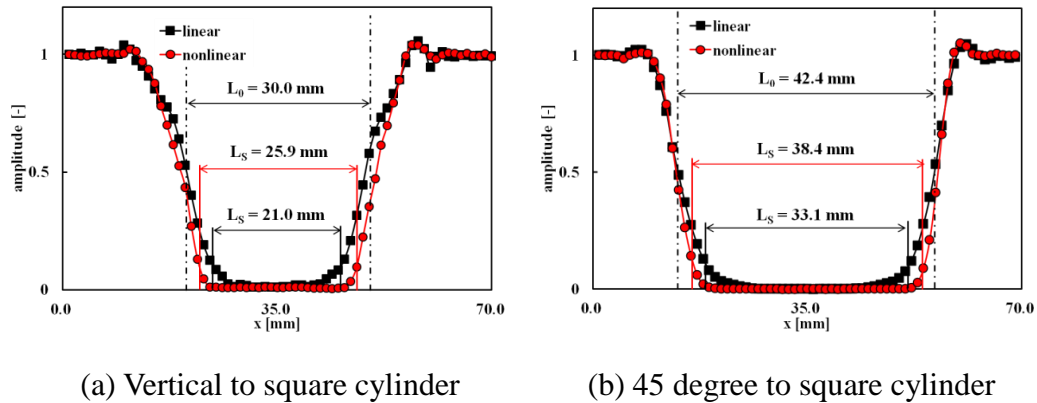
Figure 40 Signal amplitude along traversed direction.

6.4 Nonlinear shadow method with different fluid layers

To verify the effect of parametric sound enhancement technique with different fluid layers in noninvasive measurement, the experiments were carried out. A schematic of the experimental setup is shown in Figs 41 and 42, corresponding to the top view of the setup and side view of the square cylinder, respectively. The transducer and receiver are the same as that used in Section 6.1. A square cylinder made of aluminum was used for the measurement test. It was located at $z = 200$ mm in water behind the ethanol layer, and the hydrophone was at $z = 300$ mm. A sampling of the acoustic signals was carried out by traversing the cylinder manually at every 2 mm normal to the beam axis. Then, the B-mode images of the signal amplitude distribution were generated using the shadow method. Note that the primary waves were removed by a high-pass filter with a cut-off frequency of 3.5 MHz, and the envelope of the secondary wave signals was evaluated using the Hilbert transformation.

Figures 43 (a) and (b) show the B-mode images of nonlinear sound through the ethanol layer in water and that through the water layer in water, respectively. The primary frequencies were set to $f_1 = 2.0$ MHz and $f_2 = 2.4$ MHz, and the time duration of the transmission was set to 1.28 μs. Note that the B-mode

image is shown after logarithmic data compression of large amplitude differences between the direct waves and the penetration waves through the cylinder. Three types of signal amplitude distributions were observed in the results both with and without the ethanol layer. The three types of waves were penetration waves through the cylinder, reverberation waves inside the cylinder and direct waves. These distributions are more clearly observed in the result with the ethanol layer than in the water layer. The results indicate that the secondary waves from the parametric array are magnified by the ethanol layer.
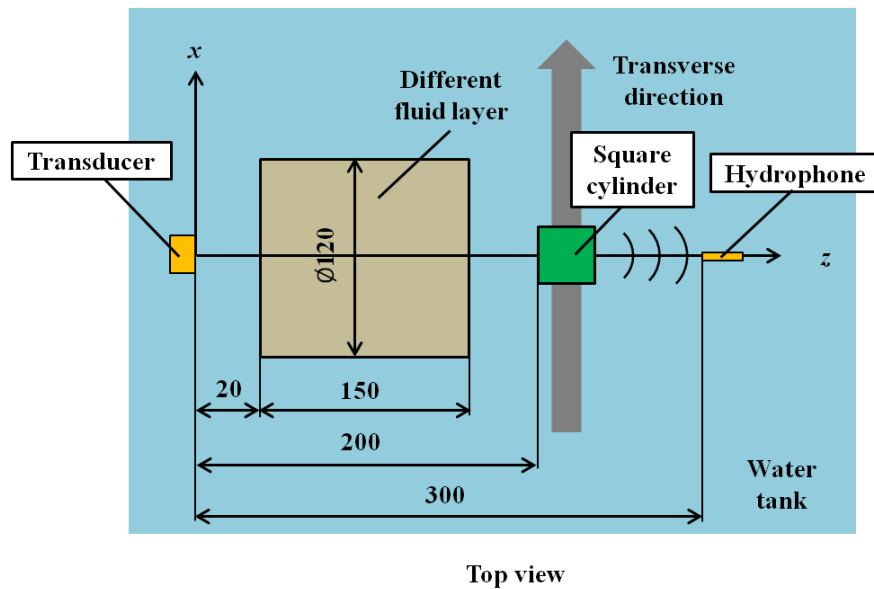
Figure 41 Schematic for noninvasive measurement of a square cylinder with different fluids.
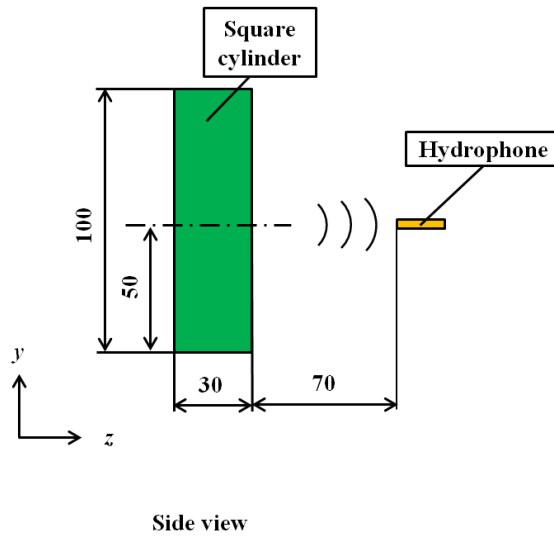
Figure 42 Side view of the square cylinder.
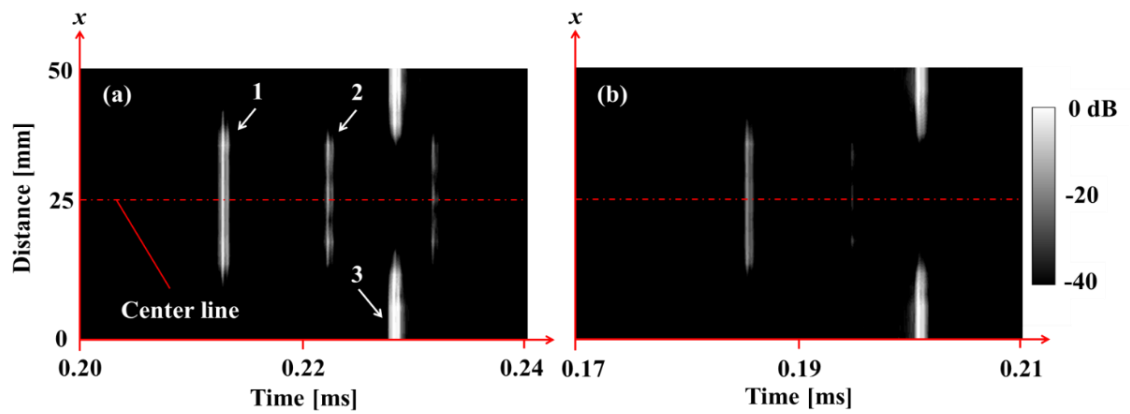
Figure 43 B-mode images after logarithmic data compression. (a) Ethanol layer and (b) Water. (1: penetration wave, 2: reverberation wave and 3: direct wave)

6. Application

To obtain the side length of the cylinder, the length is measured by following equation:

$$L_{Al} = c_{Al}t \qquad \text{Equation 52}$$

where c_{Al} = 6320 m/s is the sound speed in aluminum. Figure 44 shows the signal amplitude distributions along the centerline of the cylinder with and without the ethanol layer. The highest peak corresponds to the penetration waves through the cylinder, and the second and third peaks correspond to the reverberation waves inside the cylinder. It is clearly seen that the signal amplitudes are highly magnified in the ethanol layer compared with those in the water layer. The result indicates that the amplitude of the penetration wave is 3.7 times larger than that of the penetration wave with water, while the signal amplitude distributions are spreading in a similar manner in the lower range because of the influence of noise. It should be noted that the half width of the first peak is 0.7 mm, and that of the second peak is 0.8 mm with the ethanol layer. On the other hand, the half width of the first peak is 1.8 mm, and that of the second peak is 2.3 mm with the water layer. Then, the side length of the cylinder structure can be measured using the half distances of these peaks and the sound speed in aluminum and water. The measurement result with the ethanol layer is 29.8 ± 1.5 mm, while that in water is 29.8 ± 4.1 mm. These results indicate that the ethanol layer magnifies the amplitude of the secondary wave from the parametric array, resulting in an improvement in the size measurement accuracy of the target cylinder. Thus, the concept of the different fluid layer is useful in the noninvasive measurement of underwater structures.
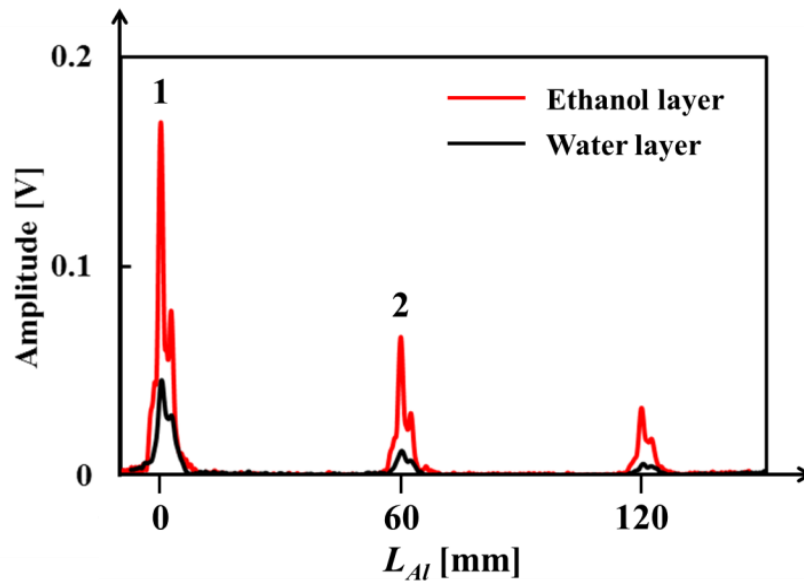
Figure 44 Variation of the signal amplitude along the centerline distance. Note that the position of the first peak is set to 0 mm.

7. Conclusion

The mechanism of nonlinear parametric sound enhancement through different fluid layers was derived theoretically, and the acoustic beam characteristic of the parametric sound at the sum and difference frequencies were numerically and experimentally studied. In addition, the concept of different fluid layer was applied to noninvasive measurement of structures in water.

First, a theoretical analysis based on the Burgers equation showed that among the five types of fluids studied, the ethanol layer in water had the highest enhancement of the secondary wave amplitudes. This was due to the nonlinear fluid properties of ethanol and the fluid/water interface. Second, to confirm the theoretical analysis, experiments were carried out by measuring the sound amplitude behind the ethanol layer in water. The experimental results showed an amplitude increase in the parametric sound at the sum frequency and second harmonics in the ethanol layer, thus supporting the theoretical results.

To predict the sound distribution and the enhancement ratio at the sum and difference frequency through the different fluid layers, a numerical simulation was conducted by solving the hybrid model that combines the fluid dynamic equations in the vicinity of sound source and the KZK equation in the far field, and the results were confirmed by hydrophone measurements. The numerical simulation and the experiments were performed using an ethanol layer in water under the irradiation of two distinct primary frequencies from a circular sound source. The results were compared with those in water to evaluate the enhancement ratios at the sum and difference frequencies. The results showed that the sound pressure at the sum and difference frequencies increases with increasing length of the different fluid layer. It was also found that the maximum enhancement ratio in the axial direction was 3.7 at a length of 150 mm at the difference frequency, which is larger than that of 2.7 at the sum frequency. The

larger enhancement ratio at the difference frequency can be attributed to the diffraction effect in the different fluid layer. Furthermore, the enhancement was the largest when the different fluid layer was positioned close to the sound source, which may be due to the large nonlinear accumulation effect in the near field occurs.

Finally, the concept of nonlinear sound enhancement through different fluid layers was applied to the noninvasive measurement of a target square cylinder in water. Nonlinear shadow method was combined with parametric sound enhancement with different fluid layers for the noninvasive detection of aluminum structure in water. The noninvasive measurement result with different fluid layer showed higher signal amplitudes in imaging and a higher accuracy of the size measurement of the target structure than conventional nonlinear shadow imaging. These results demonstrated that the concept of the different fluid layer provided a high efficiency and a high accuracy in target structure measurements in water using a parametric array, and might lead to a wider application of nonlinear acoustic imaging for high resolution underwater acoustic imaging.

Appendix A.

A - 1. Acoustic phased array

Acoustic phased array is a noninvasive measurement device featured by the beam focusing, high signal-to-noise ratio and high azimuth resolution of acoustic sound beam. The acoustic phased array has been applied to the nondestructive testing of solid materials [63, 64], medical inspection [65], under-water acoustic measurement [2], and nondestructive inspection for underwater structure using variable focusing control with phase shifts [66]. In the design of acoustic phased array, it is necessary to predict the sound pressure field emitted from the acoustic phased array for various phase shifts.

The sound propagation from the acoustic phased array in water has been studied in literature by solving the linear acoustic-wave equation with the finite difference time domain (FDTD) method [67, 68] by neglecting the nonlinear terms in the governing equation. To consider the nonlinear effect of the fluid properties, The KZK equation has been solved in the under-water acoustics, but it is not applicable to the near region of the sound source and off-axis region because the KZK equation is derived under the assumption of parabolic approximation, while near-field sound propagation is important in the beam focusing characteristics of the phased array. One of the numerical approaches applicable to the nonlinear sound propagation on the near and far field of the phased array is the method based on the fluid dynamic equation [43 - 46], while this approach has not been applied to the study of phased array in water. In this section, the nonlinear effect on sound propagation of acoustic phased array with some phase shifts was numerically studied based on the fluid dynamic equation without neglecting the nonlinear terms, and the results are compared with that of the linear acoustic-wave equation.
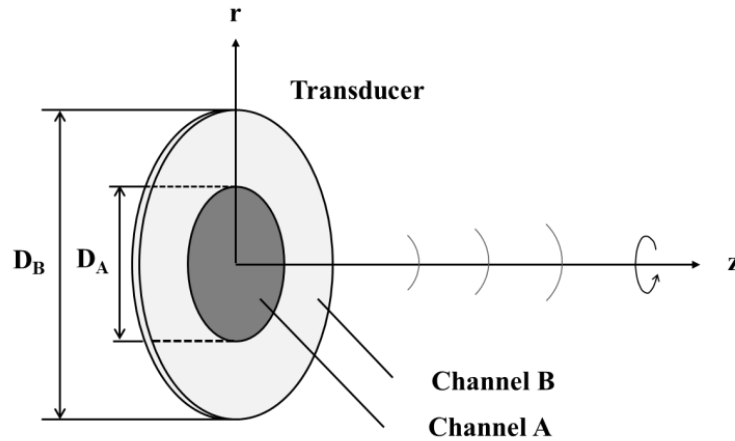
Figure 45 Schematic image of acoustic phased array.

A - 2. Numerical method

The governing equations are based on the fluid dynamic equations for viscous fluid of water as described in Section 4.2.1. They consist of mass and momentum conservation equations, entropy balance equation, state equation, in cylindrical coordinate system (r, z) under the axisymmetric assumption. These equations are solved by finite difference time domain (FDTD) based method as described in Section 4.2.1.

A - 3. Results and discussions

The numerical calculation is carried out for the sound propagation on an acoustic phased array with the radius of circular disk $D_A = 2$ cm for channel A (inner disk) and $D_B = 4$ cm for channel B (outer ring), which is illustrated in Fig 45. The computational domain is 180×180 mm in axial and radial directions, respectively, surrounded by Mur's absorbing boundary condition to avoid the reflection of the sound at the boundaries [69]. The physical properties of water used in this study are summarized in Table 2. The computational cell size is set to $\Delta = \lambda/40$ (λ: wavelength of sound) and the time increment is determined to satisfy

71

Appendix A

Courant-Friedrichs-Lewy (CFL) condition. It should be mentioned that the numerical dispersion in the FDTD based method can be considered relatively small in the range of the sound pressure amplitude.

In the numerical calculation, the acoustic pressure on the phased array is assumed uniform on the circular disk and it varies in sinusoidal form with time, as follows,

$$p = p_0 \sin\left(2\pi ft + \alpha_p\right)$$ Equation 53

where α_p is the phase shift between the transducers *A* and *B*. The frequency of the sound pressure emitted from the phased array is set to $f = 1$ MHz in the present computation.

Figures 46 and 47 show the numerical results of sound pressure distributions along the beam axis emitted from the phased array of out-of-phase and in-phase emission, respectively, where the frequency is set to $f = 1$ MHz and the pressure amplitude is $p_0 = 0.2$ MPa. Note that the out-of-phase emission corresponds to the normal phased array and the in-phase emission is the normal acoustic array. Each figure consists of contour map of the sound pressure level (a) and the pressure signal variation along the beam axis (b). The pressure amplitude of the out-of phase emission in Fig 46 is larger than that of the in-phase emission in Fig 47, which suggests the beam focusing characteristics in the out-of-phase emission. The pressure amplitude of the out-of phase emission shows the maximum amplitude at the distance 0.07 m from the sound source and it corresponds to the peak pressure amplitude of the phased array, which is slightly outside the applicable range of the KZK equation. However, pressure amplitude distribution in the in-phase emission does not show clear peak. For comparative purposes, the linear numerical calculations are carried out by neglecting the nonlinear terms and the results are shown by the contour lines of the pressure amplitude in Figs 46 and 47.

It is seen that the contour line of the linear result is deviated from the nonlinear result, and the deviation shows the nonlinear effect of the finite amplitude of the sound pressure due to the primary wave distortion, that generates higher harmonics in sound propagation. The nonlinear results shift to the higher pressure region independent of the phase shift, while the peak-to-peak amplitude remains the same as the linear results. Although there are several peaks in the pressure amplitude distribution, the largest deviation appears at the peak pressure amplitude of the phased array at the distance of 0.07 m.

In order to understand the nonlinear effect on the pressure amplitude, a normalized pressure difference of maximum pressure at the peak pressure amplitude is introduced as follows,

$$p_d = \frac{p_{N\,max} - p_{L\,max}}{p_0} \qquad \text{Equation 54}$$

where the index N and L denote the maximum pressure with and without nonlinear effect, respectively.

Figure 48 shows the variations of the normalized pressure difference at the peak pressure amplitude with respect to the source pressure amplitude for some phase shifts α_p at $f = 1$ MHz . The result indicates that the nonlinear effect appears in all phase shifts, while it is largest in the out-of-phase emission. Note that the result of phase shift $\pi/2$ is located between the results of out-of-phase and in-phase emissions. It is also found that the nonlinear effect starts around $p_0 = 0.01$ MPa and it grows abruptly with an increase in the source pressure amplitude. The nonlinear effect reaches 0.2 at $p_0 = 0.2$ MPa for the out-of phase emission, which is almost 3 times larger than the in-phase emission.

(a)   (b)
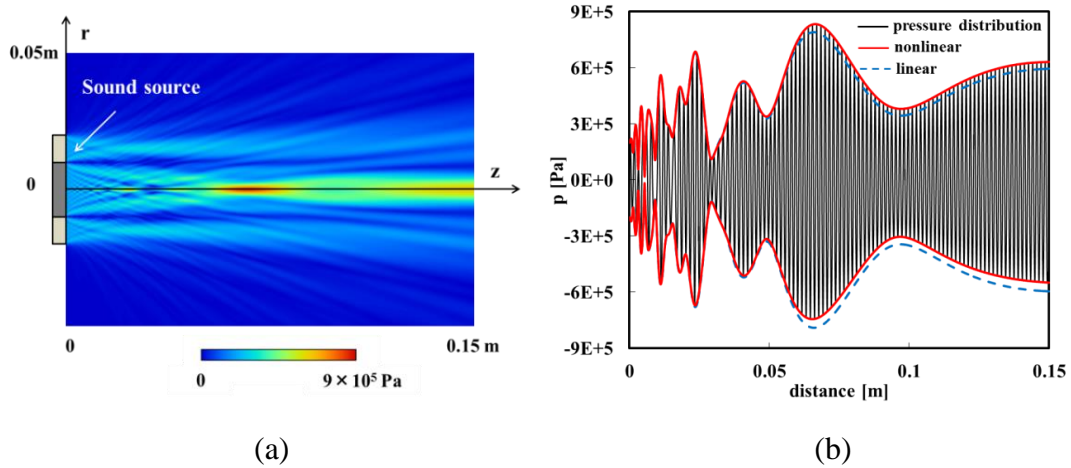
Figure 46 Sound propagation of acoustic phased array. (out-of-phase emission) (a) contour map of pressure level; (b) pressure amplitude along beam axis.

(a)   (b)
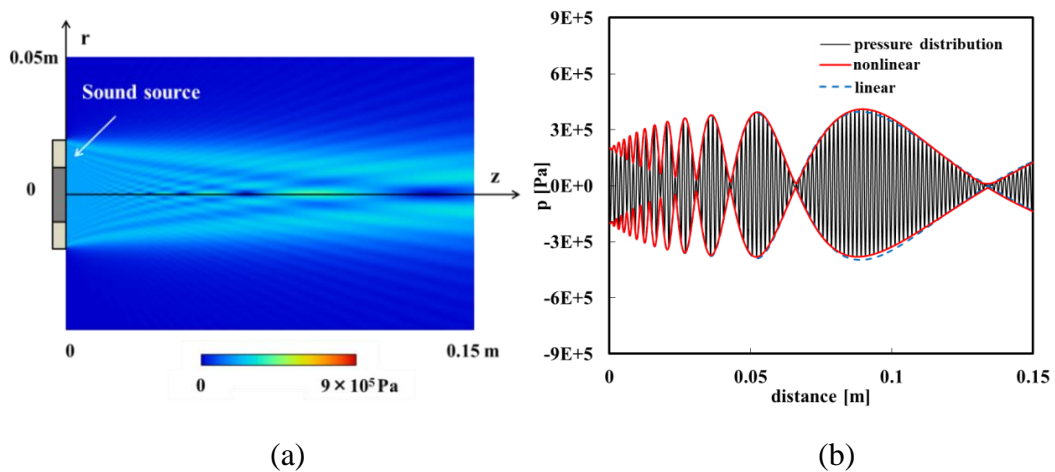
Figure 47 Sound propagation of acoustic phased array. (in-phase emission) (a) contour map of pressure level; (b) pressure amplitude along beam axis.
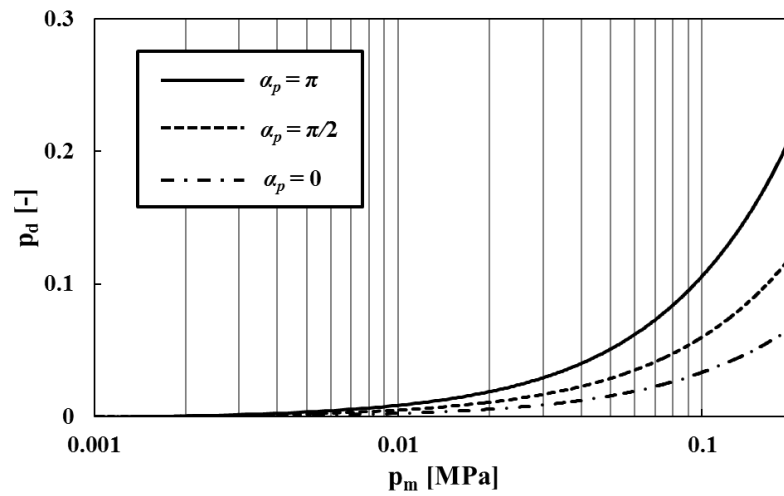
Figure 48 Variation of nonlinear effect with source pressure amplitude.

A - 4. Conclusion

The nonlinear sound propagation of acoustic phased array is numerically studied based on the fluid dynamic equations. The results with and without nonlinear terms are examined for some phase shifts to understand the influence of finite amplitude of sound pressure from the source. The present result shows that the pressure amplitude grows at the peak pressure amplitude in the out-of phase emission, while it is small in the in-phase emission. It is found that the nonlinear effect appears at the source pressure amplitude larger than 0.01 MPa in out-of-phase emission, and the growth rate increases abruptly with an increase in the source pressure amplitude.

Appendix B.

B - 1 Hybrid model and KZK equation

The hybrid model is applied to the full acoustic field of sound propagation in water emitted from a sound source, as shown in Fig 49. The numerical results of hybrid model are compared with that of the KZK equation. The computational area is 0.3 m in radial distance and 1 m in axial distance, and the radius of sound source is $a = 0.01$ m. The fluid properties of water used in the computation are as follows: sound velocity $c = 1496$ m/s, density $\rho = 0.997 \times 10^3$ kg/m^3, shear viscosity $\mu = 0.89 \times 10^{-3}$ Pa s, bulk viscosity $\eta_B = 2.4 \times 10^{-3}$ Pa s, thermal conductivity $\kappa = 0.61$ W/(m K), nonlinear coefficient $\beta = 3.5$, and diffusivity of sound $\gamma = 3.6 \times 10^{-6}$ m^2/s. The sound pressure fluctuation at the sound source is given by the sinusoidal frequency of 1 MHz and amplitude of 0.1 MPa. The absorbing boundary is used to minimize the reflection from the boundary. It should be mentioned that the interface of the hybrid model is located at $z = 0.052$ m ($= 35\lambda$, λ: wavelength) from the sound source, where the parabolic approximation is acceptable. However, the selection of the interface boundary in the far field, $z > 0.052$ m, does not change the sound pressure distribution.
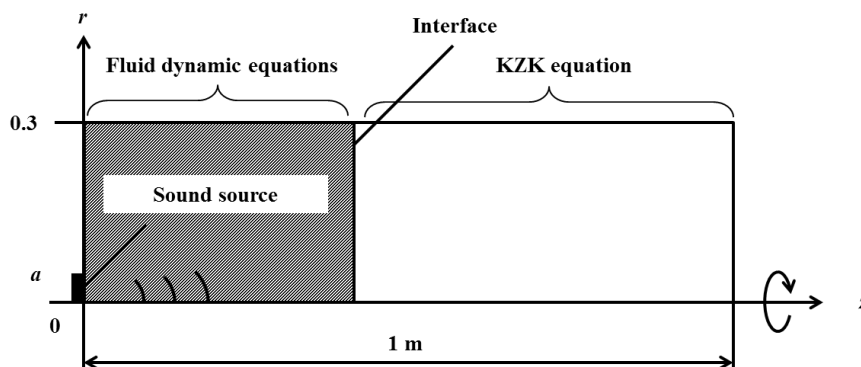

Figure 49 Schematic description of computational area.

B - 2. Results and discussion

Figure 50 shows the computational results of the fundamental harmonic (primary wave) and second harmonics of the nonlinear sound propagation in the axial direction on beam axis, which are obtained from the numerical simulation by the hybrid model and that by the KZK equation. The numerical result indicates that the sound pressure level of the hybrid model and that of the KZK equation agrees closely in the far field, while the computations in the near field deviate from each other owing to the parabolic approximation of the KZK equation. Note that the sound pressure level of the hybrid model is smoothly connected at the interface, which suggests smooth data transfer of the sound pressure at the interface of the hybrid model.

The close-up view of the near field is shown in Fig 51. It is clear that the numerical results of KZK equation shows a minor variation in sound pressure, whereas the hybrid model shows a clear variation in sound pressure near the sound source. Such variations were similarly observed in the near field of the sound source by Nomura et al. [43], who simulated the nonlinear sound pressure propagation using a fluid dynamic equations and compared their findings with numerical result of the KZK equation. The present computation was carried out using the grids (fluid dynamic equations: 3743×16040, KZK equation: 14974×1604) in the axial and radial directions, respectively, on a PC with Intel(R) Core(TM) i7-4770 CPU 3.40 GHz with OpenMP. In this case, the computational time is 14 hours with the hybrid model, while the computational time is expected to be more than 2400 hours with the fluid dynamic equations. These results indicate that the hybrid model shows a higher accuracy than the KZK equation in the near field and has a much lower computational cost than the fluid dynamic equations. Therefore, the hybrid model is an efficient tool for the study of nonlinear sound propagation in underwater acoustics.
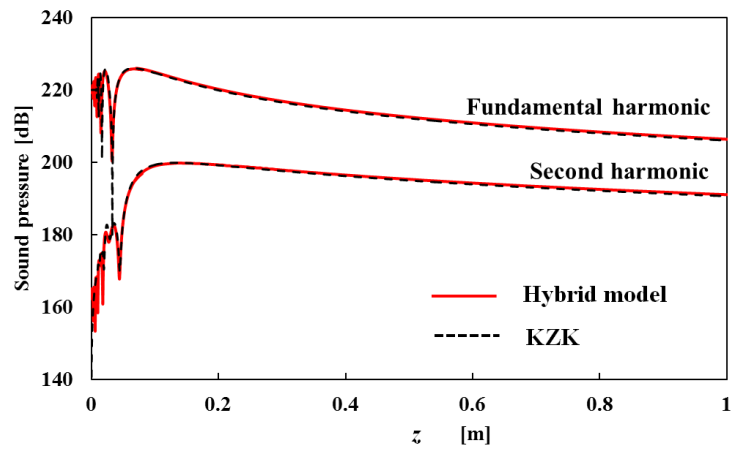
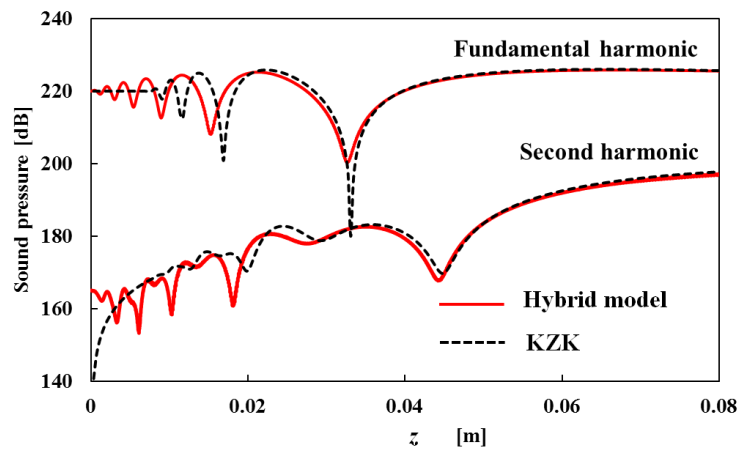Figure 50 Sound pressure distribution in full acoustic field. (0 - 1 m)

Figure 51 Sound pressure distribution near sound source. (0 - 0.08 m)

References

[1] Prieur, F., Nasholm, S. P., Austeng, A., Tichy, F., & Holm, S. (2012). Feasibility of second harmonic imaging in active sonar: measurements and simulations. *IEEE Journal of Oceanic Engineering*, *37*(3), 467-477.

[2] Humphrey, V. F. (2000). Nonlinear propagation in ultrasonic fields: measurements, modelling and harmonic imaging. *Ultrasonics*, *38*(1), 267-272.

[3] Fujisawa, K., & Asada, A. (2016). Nonlinear Acoustic Shadow Method to Reduce Reverberation Artifact. *Journal of Flow Control, Measurement & Visualization*, *4*(02), 49.

[4] Hoseini, M. R., Zuo, M. J., & Wang, X. (2013). Using ultrasonic pulse-echo B-scan signals for estimation of time of flight. *Measurement*, *46*(9), 3593-3599.

[5] Jhang, K. Y. (2000). Applications of nonlinear ultrasonics to the NDE of material degradation. *IEEE transactions on ultrasonics, ferroelectrics, and frequency control*, *47*(3), 540-548.

[6] Lee, T. H., & Jhang, K. Y. (2009). Experimental investigation of nonlinear acoustic effect at crack. *NDT & E International*, *42*(8), 757-764.

[7] Matlack, K. H., Bradley, H. A., Thiele, S., Kim, J. Y., Wall, J. J., Jung, H. J., ... & Jacobs, L. J. (2015). Nonlinear ultrasonic characterization of precipitation in 17-4PH stainless steel. *NDT & E International*, *71*, 8-15.

[8] Li, N., Sun, J., Jiao, J., Wu, B., & He, C. (2016). Quantitative evaluation of micro-cracks using nonlinear ultrasonic modulation method. *NDT & E International*, *79*, 63-72.

[9] Westervelt, P. J. (1963). Parametric acoustic array. *The Journal of the Acoustical Society of America*, *35*(4), 535-537.

[10] Berktay, H. O. (1965). Possible exploitation of non-linear acoustics in underwater transmitting applications. *Journal of Sound and Vibration*, *2*(4),

References

435-461.

[11] Muir, T. G., & Willette, J. G. (1972). Parametric acoustic transmitting arrays. *The Journal of the Acoustical Society of America*, *52*(5B), 1481-1486.

[12] Muir, T. G. (1980). Nonlinear effects in acoustic imaging. In *Acoustical imaging* (pp. 93-109). Springer US.

[13] Shen, C. C., & Lin, C. H. (2012). Chirp-encoded excitation for dual-frequency ultrasound tissue harmonic imaging. *IEEE transactions on ultrasonics, ferroelectrics, and frequency control*, *59*(11).

[14] Kozaczka, E., Grelowska, G., Kozaczka, S., & Szymczak, W. (2013). Detection of objects buried in the sea bottom with the use of parametric echosounder. *Archives of Acoustics*, *38*(1), 99-104.

[15] Wunderlich, J., Wendt, G., & Müller, S. (2005). High-resolution echo-sounding and detection of embedded archaeological objects with nonlinear sub-bottom profilers. *Marine Geophysical Researches*, *26*(2-4), 123-133.

[16] Duck, F. A. (2002). Nonlinear acoustics in diagnostic ultrasound. *Ultrasound in medicine & biology*, *28*(1), 1-18.

[17] Whalley, G. A., Gamble, G. D., Walsh, H. J., Wright, S. P., Agewall, S., Sharpe, N., & Doughty, R. N. (2004). Effect of tissue harmonic imaging and contrast upon between observer and test–retest reproducibility of left ventricular ejection fraction measurement in patients with heart failure. *European journal of heart failure*, *6*(1), 85-93.

[18] Tranquart, F., Grenier, N., Eder, V., & Pourcelot, L. (1999). Clinical use of ultrasound tissue harmonic imaging. *Ultrasound in medicine & biology*, *25*(6), 889-894.

[19] Tichy, F. E., Solli, H., & Klaveness, H. (2003). Non-linear effects in a 200-kHz sound beam and the consequences for target-strength measurement. *ICES Journal of Marine Science: Journal du Conseil*, *60*(3), 571-574.

[20] Guiroy, A., Novell, A., Ringgaard, E., Lou-Moeller, R., Gregoire, J. M.,

References

Abellard, A. P., ... & Levassort, F. (2013). Dual-frequency transducer for nonlinear contrast agent imaging. *IEEE transactions on ultrasonics, ferroelectrics, and frequency control*, *60*(12), 2634-2644.

[21] Harput, S., McLaughlan, J., Cowell, D. M., & Freear, S. (2014). Superharmonic imaging with chirp coded excitation: Filtering spectrally overlapped harmonics. *IEEE transactions on ultrasonics, ferroelectrics, and frequency control*, *61*(11), 1802-1814.

[22] De Robertis, A., McKelvey, D. R., & Ressler, P. H. (2010). Development and application of an empirical multifrequency method for backscatter classification. *Canadian Journal of Fisheries and Aquatic Sciences*, *67*(9), 1459-1474.

[23] Di Marcoberardino, L., Marchal, J., & Cervenka, P. (2011). Nonlinear multi-frequency transmitter for seafloor characterization. *Acta Acustica united with Acustica*, *97*(2), 202-208.

[24] Baker, A. C. (1992). Nonlinear pressure fields due to focused circular apertures. *The Journal of the Acoustical Society of America*, *91*(2), 713-717.

[25] Kishi, N., Asada, A., Abukawa, K., & Fujisawa, K. (2015, February). Inspection methods for underwater structures of ports and harbors. In *Underwater Technology (UT), 2015 IEEE* (pp. 1-5). IEEE.

[26] Fujisawa, K., & Asada, A. (2015). Nonlinear sound propagation on acoustic phased array. *Applied Acoustics*, *95*, 57-59.

[27] Leighton, T. (2012). *The acoustic bubble*. Academic press.

[28] Stride, E., & Saffari, N. (2003). Microbubble ultrasound contrast agents: a review. *Proceedings of the Institution of Mechanical Engineers, Part H: Journal of Engineering in Medicine*, *217*(6), 429-447.

[29] Doc, J. B., Conoir, J. M., Marchiano, R., & Fuster, D. (2016). Nonlinear acoustic propagation in bubbly liquids: Multiple scattering, softening and hardening phenomena. *The Journal of the Acoustical Society of America*, *139*(4), 1703-1712.

References

[30] Hashiba, K., & Masuzawa, H. (2003). Effect of micro-bubbles in water on beam patterns of parametric array. *Japanese journal of applied physics*, *42*(5S), 3227.

[31] Ryder, J. D., Rogers, P. H., & Jarzynski, J. (1976). Radiation of difference-frequency sound generated by nonlinear interaction in a silicone rubber cylinder. *The Journal of the Acoustical Society of America*, *59*(5), 1077-1086.

[32] Cobb, W. N. (1983). Finite amplitude method for the determination of the acoustic nonlinearity parameter B/A. *The Journal of the Acoustical Society of America*, *73*(5), 1525-1531.

[33] Beyer, R. T. (1960). Parameter of nonlinearity in fluids. *The Journal of the Acoustical Society of America*, *32*(6), 719-721.

[34] Law, W. K., Frizzell, L. A., & Dunn, F. (1981). Ultrasonic determination of the nonlinearity parameter B/A for biological media. *The Journal of the Acoustical Society of America*, *69*(4), 1210-1212.

[35] Maraghechi, B., Hasani, M. H., Kolios, M. C., & Tavakkoli, J. (2016). Temperature dependence of acoustic harmonics generated by nonlinear ultrasound wave propagation in water at various frequencies. *The Journal of the Acoustical Society of America*, *139*(5), 2475-2481.

[36] Fujisawa, K., & Asada, A. (2016). Nonlinear parametric sound enhancement through different fluid layer and its application to noninvasive measurement. *Measurement*, *94*, 726-733.

[37] Burgers, J. M. (1948). A mathematical model illustrating the theory of turbulence. *Advances in applied mechanics*, *1*, 171-199.

[38] Blackstock, D. T. (1985). Generalized Burgers equation for plane waves. *The Journal of the Acoustical Society of America*, *77*(6), 2050-2053.

[39] Zabolotskaya, E. A. & Khokhlov, R. V. (1969). Quasi-plane waves on the nonlinear acoustics of confined beams. *Soviet physics. Acoustics.*, **15**, 35-40.

[40] Kuznetsov, V. P. (1971). Equation of nonlinear acoustics. *Soviet physics.*

References

Acoustics., **16**, 467-470.

[41] Aanonsen, S. I. (1983). Numerical computation of the nearfield of a finite amplitude sound beam. University of Bergen, Department of Applied Mathematics.

[42] Kamakura, T., Akiyama, M., & Aoki, K. (2004). A higher-order parabolic equation for describing nonlinear propagation of ultrasound beams. *Acoustical Science and Technology*, *25*(2), 163-165.

[43] Nomura, H., Hedberg, C. M., & Kamakura, T. (2012). Numerical simulation of parametric sound generation and its application to length-limited sound beam. *Applied Acoustics*, *73*(12), 1231-1238.

[44] Fujisawa, K., & Asada, A. (2016). Numerical study on nonlinear acoustic pulse propagation for parametric array with different fluid layer. *Bulletin of the American Physical Society*, *61*.

[45] Fujisawa, K., & Asada, A. (2014, November). Numerical analysis of sound propagation for acoustic lens array in different fluid mediums. In *APS Meeting Abstracts*.

[46] Fujisawa, K. (2014). Numerical Study on Nonlinear Sound Propagation for Parametric Array. *Journal of Flow Control, Measurement & Visualization*, *2014*.

[47] Hallaj, I. M., & Cleveland, R. O. (1999). FDTD simulation of finite-amplitude pressure and temperature fields for biomedical ultrasound. *The Journal of the Acoustical Society of America*, *105*(5), L7-L12.

[48] Fujisawa, K., & Asada, A. (2015). Numerical method for calculating nonlinear sound propagation in full acoustic field. *Acoustical Science and Technology*, *36*(5), 438-440.

[49] Qi, Q., & Geers, T. L. (1998). Evaluation of the perfectly matched layer for computational acoustics. *Journal of Computational Physics*, 139(1), 166-183.

[50] Pinkerton, J. M. M. (1947). A pulse method for the measurement of ultrasonic absorption in liquids: results for water. *Nature*, *160*(4056),

References

128-129.

[51] Carlin, B. Ultrasonics, 1960.

[52] Blitz, J., & Simpson, G. (1995). *Ultrasonic methods of non-destructive testing* (Vol. 2). Springer Science & Business Media.

[53] Wróbel, G., & Pawlak, S. (2007). A comparison study of the pulseecho and through-transmission ultrasonics in glass/epoxy composites. *Journal of Achievements in Materials and Manufacturing Engineering*, *22*(2), 51-54.

[54] Tattersall, H. G. (1973). The ultrasonic pulse-echo technique as applied to adhesion testing. *Journal of Physics D: Applied Physics*, *6*(7), 819.

[55] Krautkrämer, J., & Krautkrämer, H. (2013). *Ultrasonic testing of materials*. Springer Science & Business Media.

[56] Purnell, P., Gan, T. H., Hutchins, D. A., & Berriman, J. (2004). Noncontact ultrasonic diagnostics in concrete: A preliminary investigation. *Cement And Concrete Research*, *34*(7), 1185-1188.

[57] Song, H. W., & Saraswathy, V. (2007). Corrosion monitoring of reinforced concrete structures-a. *Int. J. Electrochem. Sci*, *2*, 1-28.

[58] Pinton, G., Aubry, J. F., Bossy, E., Muller, M., Pernot, M., & Tanter, M. (2012). Attenuation, scattering, and absorption of ultrasound in the skull bone. *Medical physics*, *39*(1), 299-307.

[59] Chimenti, D. E. (2014). Review of air-coupled ultrasonic materials characterization. *Ultrasonics*, *54*(7), 1804-1816.

[60]   Hoseini, M. R., Wang, X., & Zuo, M. J. (2012). Estimating ultrasonic time of flight using envelope and quasi maximum likelihood method for damage detection and assessment. *Measurement*, 45(8), 2072-2080.

[61] Wachinger, C., Klein, T., & Navab, N. (2012). The 2D analytic signal for envelope detection and feature extraction on ultrasound images. *Medical Image Analysis*, *16*(6), 1073-1084.

References

[62] Mari, J. M., & Cachard, C. (2007). Acquire real-time RF digital ultrasound data from a commercial scanner. *Electronic Journal" Technical Acoustics*, *3*.

[63] Song, S. J., Shin, H. J., & Jang, Y. H. (2002). Development of an ultra sonic phased array system for nondestructive tests of nuclear power plant components. *Nuclear engineering and design*, *214*(1), 151-161.

[64] Ye, J., Kim, H. J., Song, S. J., Kang, S. S., Kim, K., & Song, M. H. (2011). Model-based simulation of focused beam fields produced by a phased array ultrasonic transducer in dissimilar metal welds. *NDT & E International*, *44*(3), 290-296.

[65] Saito, Y., Tsuchiya, T., & Endoh, N. (2006). Numerical analysis of temperature rise in tissue using electronically focused ultrasound. *Japanese journal of applied physics*, *45*(5S), 4693.

[66] Abukawa, K., Igarashi, T., & Asada, A. (2012, October). Three-dimension diagnostic methods of quay wall using focusing acoustic parametric probe and imaging sonar. In *2012 Oceans* (pp. 1-4). IEEE.

[67] Iijima, F., Tsuchiya, T., & Endoh, N. (2000). Analysis of characteristics of underwater sound propagation in the ocean by a finite difference time domain method. *Japanese Journal of Applied Physics*, *39*(5S), 3200.

[68] Mori, K., Nakamura, T., Yokoyama, T., & Hasegawa, A. (2005). 3-D FDTD analysis of sound field focused by biconcave acoustic lens for normal incidence. *Japanese journal of applied physics*, *44*(6S), 4696.

[69] Mur, G. (1981). Absorbing boundary conditions for the finite-difference approximation of the time-domain electromagnetic-field equations. *IEEE transactions on Electromagnetic Compatibility*, (4), 377-382.